Article

Cell

53BP1 and the LINC Complex Promote Microtubule-Dependent DSB Mobility and DNA Repair

Graphical Abstract

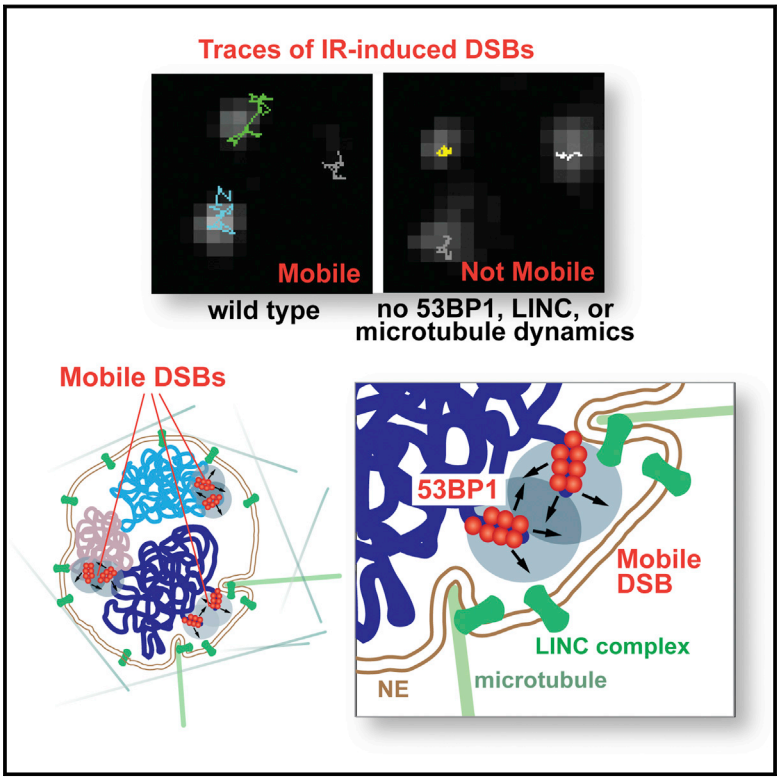

Authors

Francisca Lottersberger, Roos Anna Karssemeijer, Nadya Dimitrova, Titia de Lange

Correspondence

delange@rockefeller.edu

In Brief

Increased chromatin mobility at sites of double-stranded breaks is mediated by 53BP1, SUN1/2 in the nuclear envelope, and microtubule dynamics and contributes to aberrant DNA repair in cells with multiple DNA breaks.

Highlights

- Dysfunctional telomeres and DSBs are more mobile than undamaged chromatin
- 53BP1, the LINC complex, and dynamic microtubules are required for DSB mobility
- DSB mobility promotes radial formation in PARPi-treated BRCA1-deficient cells
- DSB mobility is proposed to represent an error correction mechanism

Lottersberger et al., 2015, Cell *163*, 880–893
November 5, 2015
http://dx.doi.org/10.1016/j.cell.2015.09.057

CellPress

Cell

Article

53BP1 and the LINC Complex Promote Microtubule-Dependent DSB Mobility and DNA Repair

Francisca Lottersberger,[1] Roos Anna Karssemeijer,[1] Nadya Dimitrova,[1,2] and Titia de Lange[1,*]

[1]Laboratory for Cell Biology and Genetics, The Rockefeller University, 1230 York Avenue, New York, NY 10065, USA

[2]Present address: Department for Molecular, Cellular, and Developmental Biology, Yale University, 219 Prospect Street, New Haven, CT 06511, USA

*Correspondence: delange@rockefeller.edu

http://dx.doi.org/10.1016/j.cell.2015.09.057

SUMMARY

Increased mobility of chromatin surrounding double-strand breaks (DSBs) has been noted in yeast and mammalian cells but the underlying mechanism and its contribution to DSB repair remain unclear. Here, we use a telomere-based system to track DNA damage foci with high resolution in living cells. We find that the greater mobility of damaged chromatin requires 53BP1, SUN1/2 in the linker of the nucleoskeleton, and cytoskeleton (LINC) complex and dynamic microtubules. The data further demonstrate that the excursions promote non-homologous end joining of dysfunctional telomeres and implicated Nesprin-4 and kinesins in telomere fusion. 53BP1/LINC/microtubule-dependent mobility is also evident at irradiation-induced DSBs and contributes to the mis-rejoining of drug-induced DSBs in BRCA1-deficient cells showing that DSB mobility can be detrimental in cells with numerous DSBs. In contrast, under physiological conditions where cells have only one or a few lesions, DSB mobility is proposed to prevent errors in DNA repair.

INTRODUCTION

The integrity of eukaryotic genomes is perpetually threatened by the formation of double-stranded breaks (DSBs), which can arise due to errors in DNA metabolism or genotoxic insults, such as chemotherapeutic agents. The repair of DSBs is a critical aspect of genome maintenance, despite the fact that non-cycling cells experience only a few DSBs per day (Fumagalli et al., 2012; U. Herbig, personal communication). In G1, DSBs are repaired by non-homologous end-joining (NHEJ) whereas replicating cells can also use a second pathway, homology-directed repair (HDR), to restore genome integrity. NHEJ and HDR are highly regulated to avoid ectopic repair, which can generate translocations, multicentric chromosomes, and other deleterious chromosome rearrangements.

The role of the DNA damage response factor 53BP1 in DSB repair and its contribution to cell-cycle appropriate execution of NHEJ and HDR has been studied extensively (reviewed in Escribano-Díaz et al., 2013; Panier and Boulton, 2014; Zimmermann and de Lange, 2014). 53BP1 accumulates at sites of DNA damage through a dual interaction between its Tudor domain with constitutively dimethylated histone H4 (H4K20diMe) and its UDR domain with ubiquitylated histone H2A (H2AK15Ub), which marks sites of DNA damage. Many of the functions of 53BP1 are mediated by binding partners that associate with the 53BP1 N terminus upon phosphorylation of ST/Q sites by the ataxia telangiectasia mutated (ATM) and ataxia telangiectasia and Rad3 related (ATR) kinases.

A critical role of 53BP1 is to limit the 5′ resection of the broken ends in a cell-cycle-dependent manner. Whereas inappropriate resection in G1 will impede the repair of DSBs by NHEJ, resection is needed for HDR in S/G2. Inhibition of 5′ end resection in G1 is primarily mediated by the 53BP1-bound Rif1 and Rev7/MAD2L2, but the mechanism by which resection is blocked is unknown (Chapman et al., 2013; Di Virgilio et al., 2013; Escribano-Díaz et al., 2013; Feng et al., 2013; Zimmermann et al., 2013; Boersma et al., 2015; Xu et al., 2015). In S/G2, the action of Rif1 and Rev7/MAD2L2 are counteracted by BRCA1, allowing resection and generating the 3′ overhangs required for HDR. A second 53BP1-interacting factor, PTIP, has an auxiliary role that involves end trimming by the Artemis nuclease (Munoz et al., 2007; Callen et al., 2013; Wang et al., 2014).

The contribution of 53BP1 to DSB repair pathway choice has received considerable attention in the context of the treatment of BRCA1-deficient cancers with poly(ADP-ribose) polymerase inhibitors (PARPi) (reviewed in Banerjee et al., 2010). PARP inhibition results in a large number of persistent single-stranded (ss) gaps that are converted into DSBs by DNA replication. In absence of BRCA1, the inefficiency of 5′ end resection allows NHEJ to dominate the repair. When many broken ends persist, NHEJ can promote mis-rejoining of broken chromatids, forming radial chromosomes and chromosome aberrations that have lethal consequences. This mis-repair of DSBs determines the synthetic lethality of PARP inhibition and HR deficiency. Removal of 53BP1 in this setting blocks the formation of mis-repaired chromosomes, in part by alleviating the inhibition of resection and hence restoring HDR (Cao et al., 2009; Bouwman et al., 2010; Bunting et al., 2010; Chapman et al., 2013; Di Virgilio et al., 2013; Zimmermann et al., 2013; Xu et al., 2015). Indeed, absence of Rif1 or MAD2L2 also minimizes the formation of mis-repaired chromosomes in PARPi-treated BRCA1-negative cells. However, 53BP1 has a greater effect than Rif1 (Zimmermann et al.,

2013), suggesting a second mechanism by which 53BP1 promotes mis-rejoining.

We have used dysfunctional telomeres to investigate the second, Rif1-independent function of 53BP1. Mammalian telomeres are protected from the DNA damage response (DDR) by the six-member shelterin protein complex residing on the telomeric TTAGGG repeats (reviewed in Palm and de Lange, 2008). Removal of TRF2 from shelterin unleashes two pathways that normally are repressed at telomeres. Telomeres lacking TRF2 activate ATM kinase signaling, leading to Chk2 phosphorylation and the accumulation of 53BP1 at telomeres. In addition, TRF2 loss from telomeres renders them highly susceptible to Ku70/80- and DNA ligase IV (lig4)-dependent classical(c)-NHEJ.

In addition to blocking resection at dysfunctional telomeres, 53BP1 alters their mobility. After loss of TRF2, telomeres travel greater distances and roam larger subnuclear territories than functional telomeres (Dimitrova et al., 2008). This effect was also observed upon telomere deprotection with a TIN2 short hairpin RNA (shRNA) (Chen et al., 2013). The altered mobility of dysfunctional telomeres is strictly dependent on 53BP1 but not influenced by Rif1 (Zimmermann et al., 2013) or Rev7/MAD2L2 (Boersma et al., 2015). Given that, in G1, the fusion of two telomeres involves chromosome ends that are spatially separated, we speculated that 53BP1-dependent mobility could stimulate c-NHEJ by increasing the chance that two ends become juxtaposed. Indeed, 53BP1 is required for telomere-telomere fusions (Dimitrova et al., 2008) and this dependency cannot be fully explained by the ability of 53BP1 to block resection (Zimmermann et al., 2013).

In budding yeast, increased chromatin mobility occurs near an I-Sce-induced DSB and, to lesser extent, at the level of global chromatin (Dion et al., 2012; Miné-Hattab and Rothstein, 2012; Seeber et al., 2013), possibly enhancing the homology search needed for HDR (Agmon et al., 2013). Similarly, in fission yeast, DSBs associate with the LINC complex in a process that promotes HDR (Swartz et al., 2014). However, the data on the mobility of DSBs in mammalian cells has been equivocal (reviewed in Dion and Gasser, 2013). Ionizing radiation (IR)-induced DSBs show an ATM-dependent increase in mobility (Neumaier et al., 2012; Becker et al., 2014), lesions induced by α-particles or I-PpoI have been inferred to move (Aten et al., 2004; Falk et al., 2007; Gandhi et al., 2012), and directed movement occurs during telomere recombination in the context of the alternative lengthening of telomeres (ALT) pathway (Cho et al., 2014). However, other findings have argued against an altered mobility of DSBs (Kruhlak et al., 2006; Soutoglou et al., 2007; Jakob et al., 2009).

Using time-lapse imaging of conditional TRF2 knockout (KO) mouse embryonic fibroblasts (MEFs) as a model system, we demonstrate here that 53BP1-dependent chromatin mobility is mediated by microtubules and the LINC complex. The LINC complex spans the inner and outer membranes (INM and ONM, respectively) of the nuclear envelope (NE) and connects components of the cytoskeleton, including microtubules, with the inside of the nucleus such that cytoskeletal forces are transferred to the nuclear content (reviewed in Starr and Fridolfsson, 2010; Wilson and Foisner, 2010; Chang et al., 2015). The key components of the mammalian LINC complex are the *trans*-membrane SUN-domain proteins, SUN1 and SUN2, which span the INM and interact with the KASH-domain nesprin proteins in the lumen of the NE. Nesprins cross the ONM and connect to cytoplasmic filaments, including microtubules. Using microtubule poisons in combination with SUN1/2 and kinesin KO MEFs, we show that the 53BP1-dependent mobility of dysfunctional telomeres is a LINC/microtubule-dependent process that promotes NHEJ. Furthermore, we document that the same 53BP1/LINC/microtubule-dependent mechanism promotes the mobility of IR-induced DSBs and contributes to their mis-repair in PARPi-treated BRCA1-deficient cells. These results establish a feature of the DDR that can lead to aberrant DNA repair when cells sustain large numbers of breaks. We argue that this potentially dangerous system is adaptive in the context of the physiological DDR, which has evolved to ensure correct DNA repair in cells with few DSBs.

RESULTS

A Standardized Method for Analysis of Dynamic Behavior of DNA Damage Foci

The mechanism of 53BP1-dependent mobility was studied using immortalized TRF2$^{F/F}$Cre-ER^{T1} MEFs expressing an mCherry-53BP1 fusion protein that contains the Tudor, UDR, and oligomerization domains of 53BP1 (Figure 1A). This mCherry fusion accumulates at DSBs and deprotected telomeres but is neither functional nor interferes with the function of the endogenous 53BP1 (Dimitrova et al., 2008).

As expected, mCherry-BP1-2 formed foci at the dysfunctional telomeres generated by Cre-mediated deletion of TRF2 (Figures 1A–1C), allowing detection of the dynamic behavior of mCherry-marked dysfunctional telomeres using 3D time-lapse microscopy and automated tracing in deconvolved images (Figure 1D; Movie S1A). Since MEF nuclei are flat (2–4 μm in the z direction compared to 15–20 μm in x and y), the data were analyzed in 2D-maximum intensity projected images.

Although the resulting traces can be corrected for the nuclear translocation and rotation (Dimitrova et al., 2008), large-scale nuclear deformation, such as expansion, contraction, folding, and twisting, also confounds the analysis. We therefore developed a standardized method to select nuclei that do not display overt distortions. The method is based on three parameters (Figure S1) applied to the data after correcting for the translocation and rotation of the nuclei as described previously (Dimitrova et al., 2008). First, because extensive distortion of a nucleus will usually shift the geometrical center (Figure S1A, type I; Movie S2A), the maximal movement of the geometrical center (MMGC) of the nucleus was evaluated (Figure S1B). Second, to identify nuclei undergoing expansion or contractions (Figure S1A, type II; Movie S2B), the maximal difference between the average distances of the foci from the geometrical center (MΔAD) was determined (Figure S1C). Third, we identified nuclei with groups of foci moving in the same direction, which could indicate nuclear folding, twisting, or rotation (Figure S1A, type III; Movie S2C). For this determination, the percentage of foci moving in the four different quadrants of the XY projections (upper right [UR]; lower right [LR]; upper left [UL]; lower left [LL]) was determined (Figures S1D and S1E).

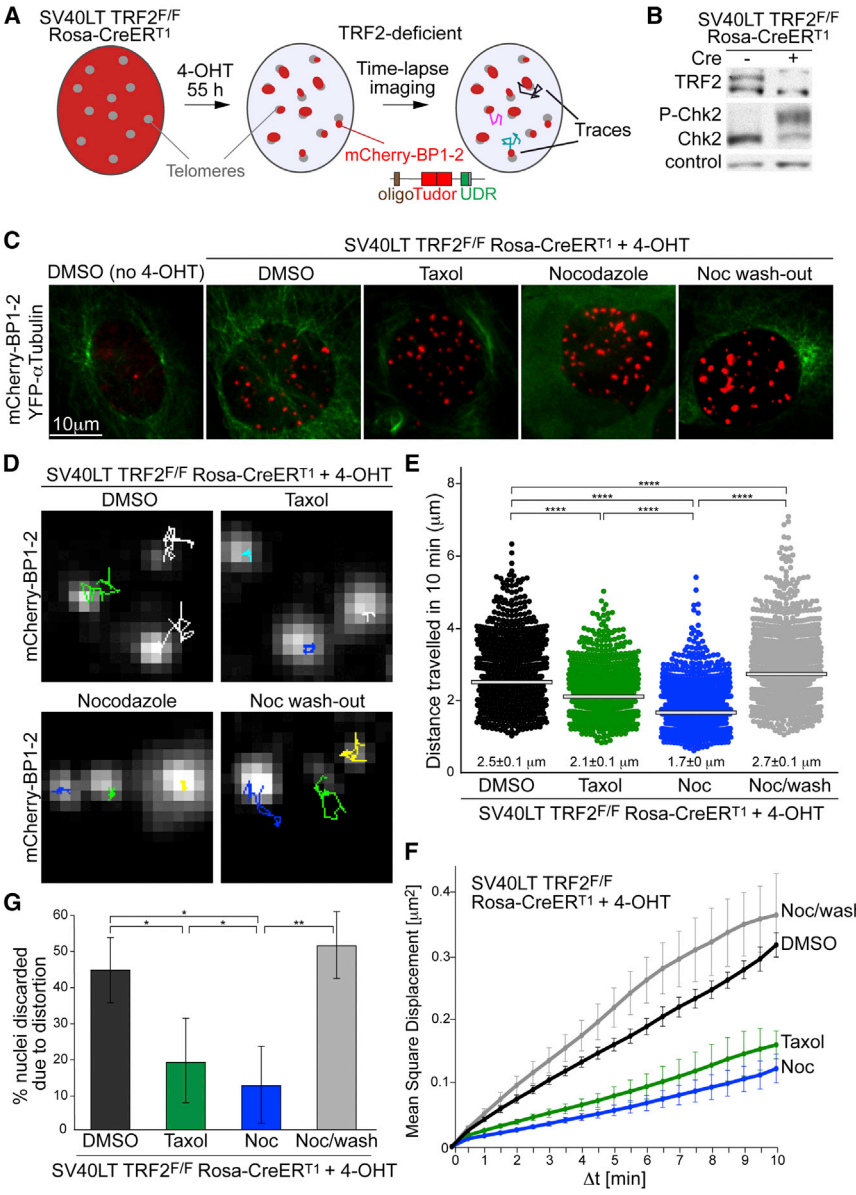

Figure 1. Microtubule Dynamics Promote Mobility of Dysfunctional Telomeres

(A) Schematic of the imaging approach. mCherry-BP1-2 foci at deprotected telomeres after TRF2 deletion were traced for 10 min by time lapse microscopy.

(B) Immunoblot for TRF2 and phosphorylation of Chk2 in TRF2$^{F/F}$ RsCre-ER^{T1} MEFs at 55–62 hr after addition of 4-OH tamoxifen (4-OHT).

(C) Images of mCherry-53BP1-2 foci with microtubule visualized with YFP-α-tubulin (with γ-correction).

(D) Examples of traces of mCherry-53BP1-2 foci as described in (B) and (C) and shown in Movies S1A–S1D.

(E and F) Distribution of the cumulative distance traveled and MSD with SDs of all the mCherry-BP1-2 foci detected in the conditions as (C). Data obtained from three independent experiments with greater than ten cells/condition. Numbers below the data points are averages and SDs of the three median values from three independent experiments. Bars represent the median of all the foci (>1,000) traced. p values are from two-tailed Mann-Whitney test. ****p < 0.0001, ***p < 0.001, **p < 0.01, *p < 0.05. ns, not significant.

(G) Percentage of cells discarded (means and SDs from three independent experiments). The p values were based on unpaired t test. Symbols as in (F).

See also Figure S1 and Table S1.

Sets of foci that show concerted movement will over-populate one of these quadrants, allowing detection of nuclei with distortions. Similarly, over-population of half the space in the projections (lateral, vertical, diagonal) was used to detect nuclear rotation. Using arbitrarily set thresholds for these parameters (Figure S1; see Experimental Procedures), nuclei were discarded from the analysis. In most experiments, approximately half the nuclei passed these selection criteria and were deemed to retain their shape.

Analysis of the selected nuclei showed that dysfunctional telomeres traveled a median cumulative distance of 2.5 μm in 10 min (Figures 1D and 1E; Table S1; Movie S1A), which is consistent with previous data (Dimitrova et al., 2008). The mean square displacement (MSD) increased over time, with a final MSD of 0.3 μm^2 after 10 min (Figure 1F; Table S1). Fitting of the MSD measured for dysfunctional telomeres to MSD = A + Γt$^{\alpha}$ showed an anomalous diffusion coefficient (α) of close to 1.0 (Table S1), indicating diffusive motion. The calculated diffusion coefficient (3.7 × 10^{-3} μm^2/s; Table S1) is in the range observed by others for dysfunctional mammalian telomeres (Chen et al., 2013; Cho et al., 2014), DNA damage lesions formed after UV and IR irradiation of mammalian cells (Kruhlak et al., 2006; Falk et al., 2007; Mahen et al., 2013; Becker et al., 2014), and a locus next to an I-SceI induced DSB in yeast (Miné-Hattab and Rothstein, 2012; Dion et al., 2012).

53BP1-Dependent Mobility Requires Dynamic Microtubules

We previously showed that the movement of dysfunctional telomeres is not affected by the actin drug, latrunculin A (Dimitrova et al., 2008). In contrast, when cells were incubated with the microtubule poisons Taxol or nocodazole, which stabilize and depolymerize microtubules, respectively (Figure 1C), there was a striking reduction in the mobility of the dysfunctional telomeres and the distance traveled by the telomeres was significantly smaller (Figures 1D-1F; Table S1; Movies S1A–S1C). The effect of nocodazole was completely reversed within 1 hr of its removal from the media, showing that the lack of dynamic behavior was

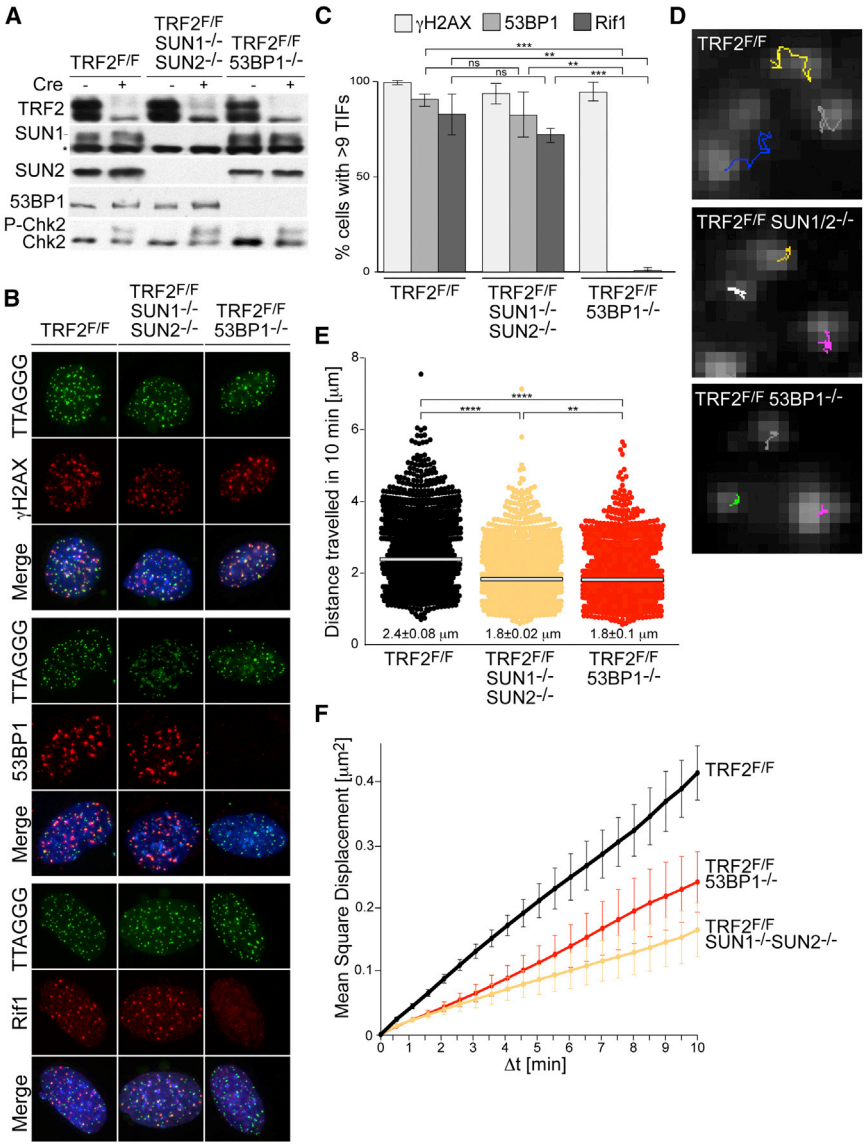

Figure 2. SUN1 and SUN2 Promote Mobility of Dysfunctional Telomeres

(A) Immunoblots for TRF2, SUN1, SUN2, 53BP1, and phosphorylated Chk2 in the indicated MEFs at 72 hr after Hit&Run Cre.

(B) Telomere dysfunction-induced foci (TIF) assay on the MEFs described in (A). Telomeres were detected by FISH with FITC-$(CCCTAA)_3$ probe (green). Phosphorylated H2AX (top panel), 53BP1 (middle panel), and Rif1 (bottom panel) were detected by IF (red). DAPI, DNA (blue).

(C) Quantification of TIF response after Cre as assayed in (B). Cells with greater than nine TIFs were scored. Values are means and SDs of three independent experiments. p values were from an unpaired t test (see legend to Figure 1).

(D) Examples of traces of mCherry-53BP1-2 foci at 66–72 hr after Cre (see Movies S3A–S3C).

(E and F) Distribution of the cumulative distance traveled and MSDs with SDs of mCherry-BP1-2 foci in the analyzed MEFs (as in D) in four experiments, as described in Figure 1.

See also Figure S2 and Table S1.

not due to a permanent toxic effect of the drug (Figures 1D–1F; Table S1; Movie S1D). Both microtubule poisons also affected the extent to which the nuclei were distorted (Figure 1G; Table S1), indicating that much of the nuclear deformation observed in these fibroblasts is microtubule-dependent.

SUN1 and SUN2 Promote the Mobility and NHEJ of Dysfunctional Telomeres

Since the involvement of microtubule dynamics suggested a link between the dysfunctional telomeres and the cytoplasm, we tested the role of the LINC complex in the movement of dysfunctional telomeres. To this end, we used SUN1 and SUN2 KO mice (Ding et al., 2007; Lei et al., 2009) to generate immortalized conditional $TRF2^{F/F}$ $SUN1^{-/-}SUN2^{-/-}$ MEFs. The absence of the two SUN proteins did not interfere with Chk2 phosphorylation or the formation of telomere dysfunction-induced foci (TIFs) containing γH2AX, 53BP1, and Rif1 after deletion of TRF2 and 53BP1 was detected by chromatin immunoprecipitation (ChIP) at dysfunctional telomeres in SUN1/2 DKO cells (Figures 2A–2C, S2A, and S2B). Nonetheless, the SUN1/2-deficient cells showed a significant reduction in the mobility of the dysfunctional telomeres (Figures 2D–2F and S2C; Table S1; Movies S3A and S3B). The effect of removal of SUN1 and SUN2 was at least as strong as the effect of absence of 53BP1 monitored in parallel experiments (Figures 2D–2F; Table S1; Movies S3C and S3B).

The percentage of nuclei that were discarded due to deformation was reduced in the absence of SUN1 and SUN2 (Figure S2C), implicating the LINC complex in the microtubule-mediated changes in nuclear shape. In contrast, 53BP1 had no effect on nuclear deformation (Figure S2C).

Importantly, in the TRF2 SUN1/2 TKO cells, the diminished mobility of the dysfunctional telomeres was accompanied by a reduction in their fusion (Figures 3A and 3B). Metaphase spreads of cells lacking SUN1 and SUN2 showed a 2-fold decrease in the NHEJ of dysfunctional telomeres at 84 hr (Figures 3B and S2B). The reduction in telomere fusions was also apparent from the diminished appearance of fused telomeric restriction fragments (Figures S2D and S2E). The difference in telomere fusion frequency with and without the SUN proteins was negligible when the assay was saturated at a later time point (108 hr). In contrast, in 53BP1-deficient cells telomere fusions remained infrequent at later time points, consistent with 53BP1 promoting telomere fusions through inhibition of resection as well as SUN1/2-dependent mobility. Since the absence of SUN1 alone affected telomere fusions less than absence of both SUN1 and SUN2

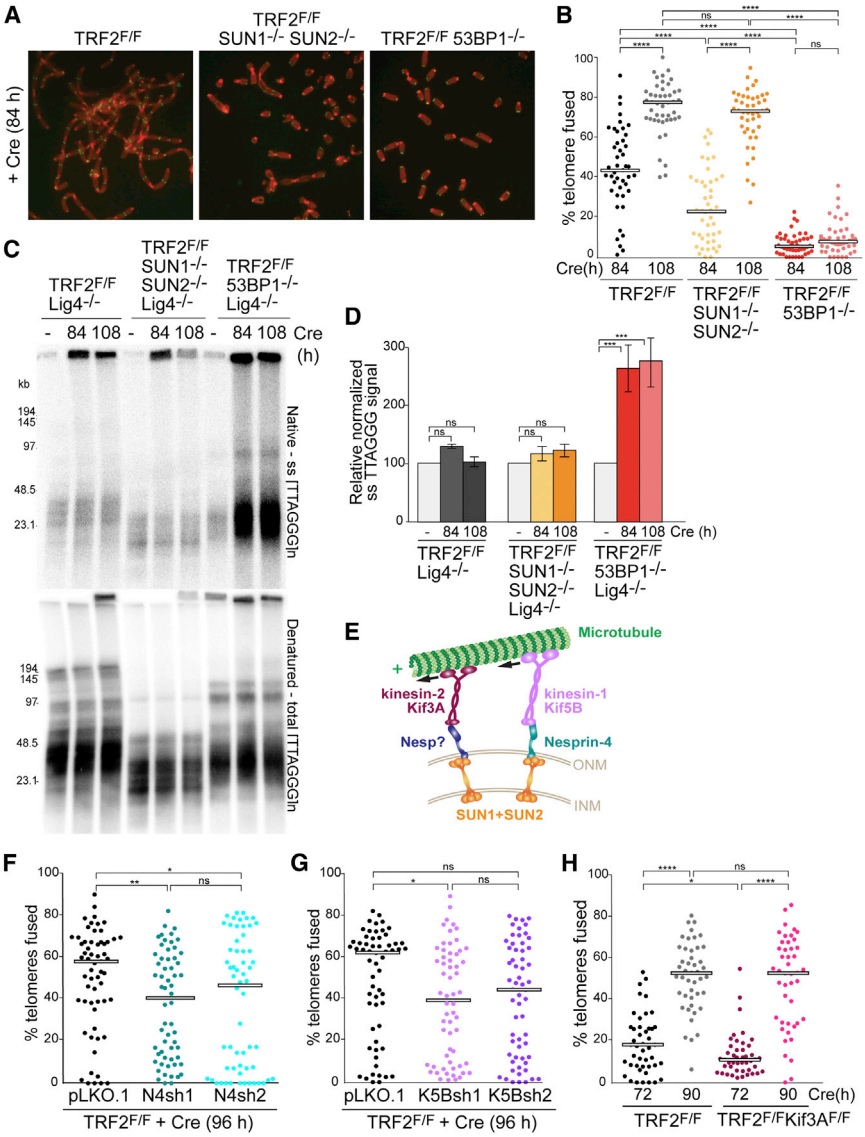

Figure 3. The LINC Complex Promotes NHEJ of Dysfunctional Telomeres

(A) Metaphases showing telomere fusions in the indicated MEFs at 84 hr after Hit&Run Cre. Telomeres were detected by FISH with a FITC-$(CCCTAA)_3$ probe (green). DNA, DAPI (red).

(B) Distribution of telomere fusions as in (A) at 84 and 108 hr after Cre. Dots represent % fusions in individual metaphases. Bars represent the median of telomere fusions in 15 metaphases for three independent experiments (45 metaphases). p values from unpaired t test (see legend to Figure 1).

(C) In-gel assay for single-stranded telomeric DNA. Telomeric overhangs detected in situ with end-labeled ^{32}P-$(AACCCT)_4$ in MboI-digested genomic DNA from the indicated MEFs at 84 and 108 hr after TRF2 deletion (top panel). Bottom: the DNA was denatured in situ and rehybridized with the same probe to determine the total telomere DNA.

(D) Quantification of relative overhang signal as detected in (C). Values represent means for four independent experiments with SDs. The ss telomeric signal was normalized to the total telomeric DNA in the same lane. For each MEF line, the normalized no Cre value of cells was set at 100 and the post-Cre values are given relative to this value. Two-way ANOVA for multiple comparisons were used to perform statistical analysis. For p value symbols see legend to Figure 1.

(E) Schematic of the LINC complex and microtubules.

(F and G) Quantification of telomere fusions in $TRF2^{F/F}$ MEFs treated with shRNAs to nesprin-4 or Kif5B 96 hr after Cre and analyzed as in (A) and (B). Bars represent the median % of telomeres fused in three independent experiments (20 metaphases each).

(H) Quantification of telomere fusions in $TRF2^{F/F}$ RsCre-ER^{T1} and $TRF2^{F/F}$ $Kif3A^{F/F}$ RsCre-ER^{T1} MEFs 72 and 90 hr after 4-OHT, as in (A) and (B). See also Figures S2 and S3.

(Figure S2F), we conclude that the SUN proteins have partially overlapping functions in this pathway.

We verified that the deficiency in telomere fusion in the SUN1/2 KO was not due to increased resection using a quantitative assay for the amount of ssTTAGGG repeats after deletion of TRF2 from SUN1/2-deficient cells. In $Lig4^{-/-}$ MEFs (TRF2/SUN1/SUN2/Lig4 quadruple KO), which are a good system for detection of resection because the telomeres remain free, there was no great increase in the overhang signal after TRF2 deletion (Figures 3C and 3D), indicating that resection remained repressed. Parallel deletion of TRF2 from $53BP1^{-/-}$ $Lig4^{-/-}$ cells showed the substantial increase in overhang signal expected from the role of 53BP1/Rif1 in repression of resection (Lottersberger et al., 2013). These data, together with the normal localization of Rif1 at dysfunctional telomeres in SUN1/2 DKO cells (Figures 2B and 2C), supports the idea that SUN1 and SUN2 are dispensable for the protection of DSBs from resection and act independently from Rif1. We propose, therefore, that SUN1 and SUN2 promote the c-NHEJ of telomeres by increasing their dynamic behavior.

Nesprin-4 and Kinesins Contribute to NHEJ of Dysfunctional Telomeres

Since the SUN proteins are connected to the cytoskeleton through nesprins (reviewed in Starr and Fridolfsson, 2010) (see Figure 3E) and SUN1/2-deficient cells lack nesprin-1, nesprin-2, nesprin-3, and nesprin-4 at the NE (Crisp et al., 2006; Padmakumar et al., 2005; Ketema et al., 2007; Lei et al., 2009; Roux et al., 2009), we tested shRNAs to nesprins for an effect on NHEJ of dysfunctional telomeres. Two shRNAs targeting nesprin-4 lowered the frequency of telomere fusions without affecting cell proliferation or the DDR (Figures 3F, S3A, and S3B).

As nesprin-4 is known to interact with the plus-end directed microtubule motor kinesin-1 (Figure 3E), we tested shRNAs to

the Kif5B subunit of kinesin-1 for an effect on the NHEJ of dysfunctional telomeres. Two shRNAs to Kif5B lowered the frequency of telomere fusions at an early time point without affecting the proliferation or the DDR upon telomere deprotection (Figures 3G, S3C, and S3D). In addition, two shRNAs to the kinesin-2 subunit Kif3A resulted in a reduced frequency of telomere fusions (Figures S4E–S4G). Since kinesin-2 had not previously been shown to cooperate with nesprin-4, we generated TRF2$^{F/F}$Kif3A$^{F/F}$ MEFs to further verify the shRNA data. Consistent with the shRNA results, MEFs lacking Kif3A showed a significant reduction in the efficiency of telomere fusions after TRF2 deletion (Figures 3G, S3H, and S3I). These data suggest that 53BP1-mediated mobility of dysfunctional telomeres likely involves redundant action by the microtubule motors kinesin-1 and kinesin-2, as well as nesprin-4 and possibly other nesprins.

Phosphorylation Sites in 53BP1 Required for Telomere Mobility

As a version of 53BP1 lacking its N-terminal S/TQ sites (53BP1-28A) fails to induce chromatin mobility (Lottersberger et al., 2013), we determined which S/TQ sites are involved in this process. We generated a collection of S or T to A mutations at the S/TQ positions in a C-terminally truncated version of 53BP1 that lacks the BRCT domain (53BP1DB; Figure 4A) (Bothmer et al., 2011) and behaves like wild-type 53BP1 in the context studied here (Lottersberger et al., 2013; Zimmermann et al., 2013). Through the analysis of the mutants, we identified one mutant, referred to as 53BP1ΔMOB, which appeared to be a separation-of-function mutant specifically deficient in the ability of 53BP1 to promote mobility but proficient in blocking resection (Figure 4A). 53BP1ΔMOB recruited Rif1 to sites of DNA damage and was able to interact with PTIP, which was expected since the region of mutated S/TQ sites falls outside the previously mapped Rif1 and PTIP interacting regions (Figures 4A and S4A–S4C) (Munoz et al., 2007; Escribano-Díaz et al., 2013). Consistent with its binding to Rif1, the 53BP1ΔMOB mutant was proficient in repressing hyper-resection at telomeres after TRF2 deletion in TRF2$^{F/F}$ 53BP1$^{-/-}$ Lig4$^{-/-}$ cells (Figures S4D and S4E).

Despite the normal interactions with Rif1 and PTIP, the ability of 53BP1ΔMOB to promote telomere fusions upon complementation of 53BP1 deficiency was significantly reduced (Figure 4B). However, 53BP1ΔMOB promoted telomere fusion similar to 53BP1DB in SUN1$^{-/-}$ SUN2$^{-/-}$ 53BP1$^{-/-}$ cells (Figures 4B and S4F), suggesting that the 53BP1ΔMOB is only deficient in a function that requires SUN1/2. Time-lapse imaging showed that 53BP1ΔMOB is completely defective in promoting the increased mobility of dysfunctional telomeres resulting in dynamics that are indistinguishable from cells transduced with the empty vector or the 53BP1Δ28A mutant (Figures 4C and S4G; Table S1). In contrast, 53BP1ΔPTIP showed no defect in promoting mobility of dysfunctional telomeres (Figures 4C and S4G; Table S1). Thus, the ability of 53BP1 to promote mobility of dysfunctional telomeres likely involves an interaction that depends on phosphorylation of one or more of the ST/Q sites in the MOB domain. The identity of the MOB domain interacting partner is unknown. It is not excluded that this domain interacts with SUN1 and SUN2 but this interaction was not detected by mass spectrometry (Di Virgilio et al., 2013) and ChIP failed to reveal SUN1 and SUN2 at dysfunctional telomeres (Figure S2A).

PTIP Is Not Required for 53BP1-Dependent Mobility

To determine whether PTIP contributes to the 53BP1-dependent mobility, TRF2 and PTIP co-deletion in SV40LT immortalized TRF2$^{F/F}$ PTIP$^{F/F}$ MEFs was analyzed. Absence of PTIP did not affect cell proliferation or the DDR at the dysfunctional telomeres (Figures S5A–S5D). In the PTIP-deficient setting, the distances traveled and MSD of the dysfunctional telomeres was equal to that of PTIP containing control cells (Figures 4D, 4F, and S5E; Table S1; Movies S4A–S4C). Moreover, the analysis of the telomere overhangs showed that PTIP deficiency did not affect the resection at dysfunctional telomeres (Figures S5F and S5G), supporting the previous conclusion that 53BP1-dependent protection from resection is primarily dependent on Rif1 (Zimmermann and de Lange, 2014). Nonetheless, as previously shown (Callen et al., 2013), telomere fusions appeared slightly delayed when PTIP was deleted (Figures 4G, S5F, and S5G). Consistent with these results, the 53BP1ΔPTIP mutant displayed a mild defect in promoting telomere fusions but appeared unaffected with regard to protection from resection and the induction of mobility (Figures 4B, 4C, S4D, and S4E).

53BP1/LINC/Microtubule-Dependent Mobility of IR-Induced DSBs

Despite their resemblance to DSBs, dysfunctional telomeres could be argued to be different from chromosome-internal DNA breaks. We therefore tested whether genome-wide DSBs are subject to the 53BP1/LINC/microtubule-dependent changes in dynamics. To this end, we analyzed the mobility of the mCherry-BP1-2 foci after induction of ~100 DSBs with 2.75 Gy IR (Rothkamm and Löbrich, 2003) in wild-type, SUN1$^{-/-}$SUN2$^{-/-}$, and 53BP1$^{-/-}$ MEFs. As expected, the Chk2 phosphorylation and formation of γ-H2AX foci were not affected by the genotype of the cells (Figures 5A–5C). The IR-induced mCherry-53BP1-2 foci showed a cumulative distance traveled and an MSD comparable to the MSD of dysfunctional telomeres. This dynamic behavior was strongly diminished in absence of 53BP1 or the SUN proteins and upon treatment with Taxol (Figures 5D–5G; Table S1; Movies S5A–S5D). Therefore, we conclude that the 53BP1/LINC/microtubules pathway promotes the mobility of chromosome-internal DSBs as it does at dysfunctional telomeres.

Undamaged Chromatin Is Minimally Affected by DSBs

We next asked whether the presence of mobile DSBs changes the dynamics of the global chromatin. To address this question, we monitored the mobility of fully functional telomeres, marked with eGFP-TRF1 in cells with and without IR-induced DSBs. The IR was delivered at 2.75 Gy, which induces ~1 DSB/60 Mb (~100 DSBs per cell, see above). Since the 80 telomeres of the mouse genome represent ~4 Mb (~0.1% of the genome), telomeres are not expected to contain DSBs after 2.75 Gy. Nonetheless, the eGFP-marked telomeres showed a very slight but statistically significant increase in the cumulative distance traveled (Figure S6). Moreover, their MSD and diffusion coefficient were slightly increased, although much less than when

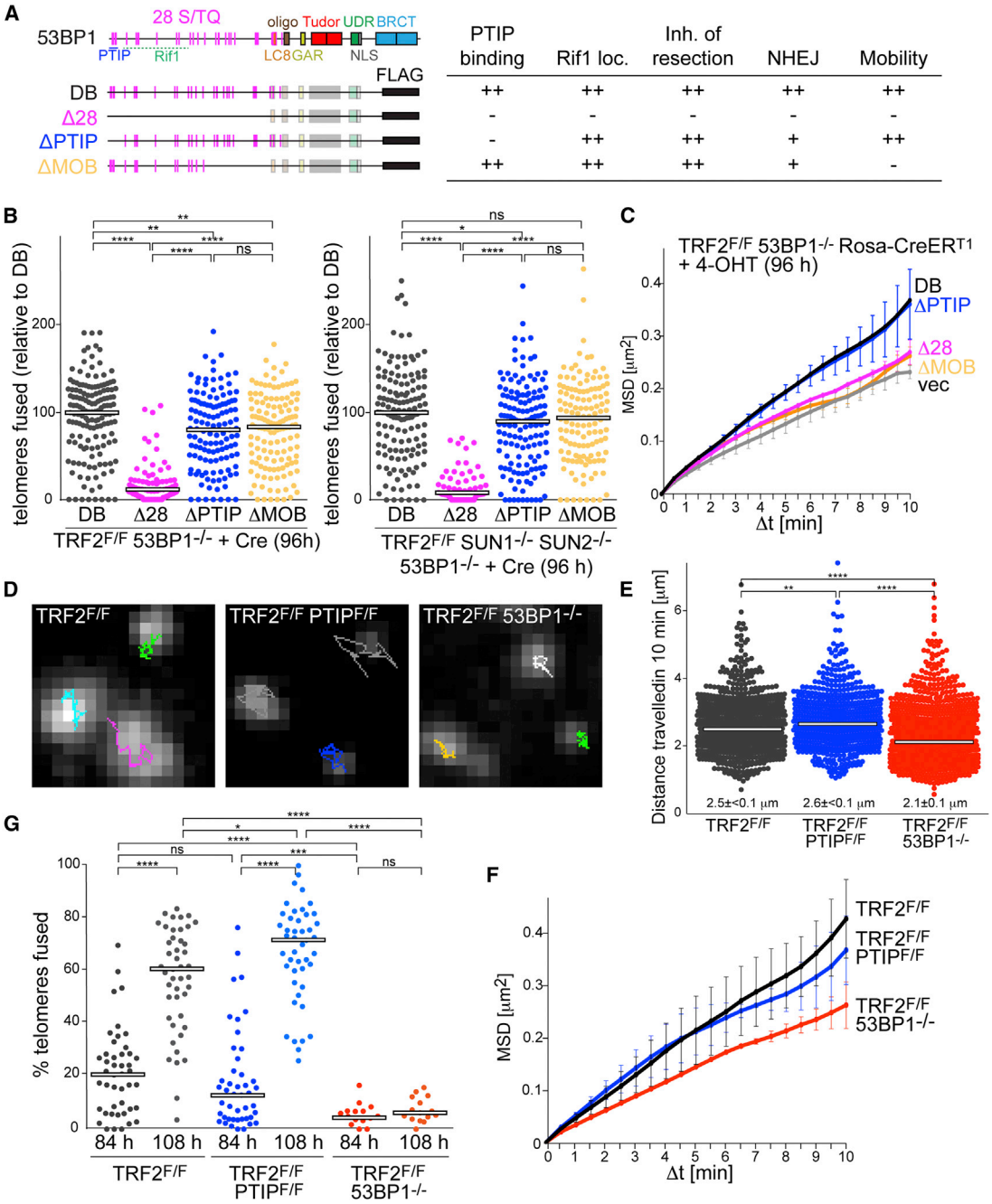

Figure 4. The Mobility Domain of 53BP1, but Not PTIP, Is Required for Mobility of Dysfunctional Telomeres

(A) Schematic of 53BP1, S/TQ site mutations, and their phenotypes.

(B) Quantification of telomere fusions in the indicated MEFs complemented with the indicated 53BP1 alleles 96 hr after TRF2 deletion with Hit&Run Cre (as in Figure 3). Data from >70 metaphases analyzed in four independent experiments. For each experiment, the median fusion frequency for 53BP1DB was set to 100 and all other values were normalized to this frequency.

(C) MSDs with SDs of mCherry-BP1-2 foci detected in the TRF2-deleted 53BP1$^{-/-}$ RsCre-ER^{T1} MEFs expressing the indicated 53BP1 alleles. Data from three independent experiments.

(D) Examples of traces of mCherry-53BP1-2 foci at 66–72 hr after Cre in the indicated MEFs (see Movies S4A–S4C).

(E and F) Distribution of the cumulative distance traveled and MSDs with SEMs of mCherry-BP1-2 foci in the indicated MEFs (as in Figure 1). Bars represent medians of the cumulative distance traveled by >500 foci in two experiments and numbers indicate the averages and SEMs of the two median values obtained in two independent experiments.

(G) Quantification of telomere fusions in the indicated MEFs at 84 and 108 hr after Cre (as in Figure 3).

See also Figures S4 and S5 and Table S1.

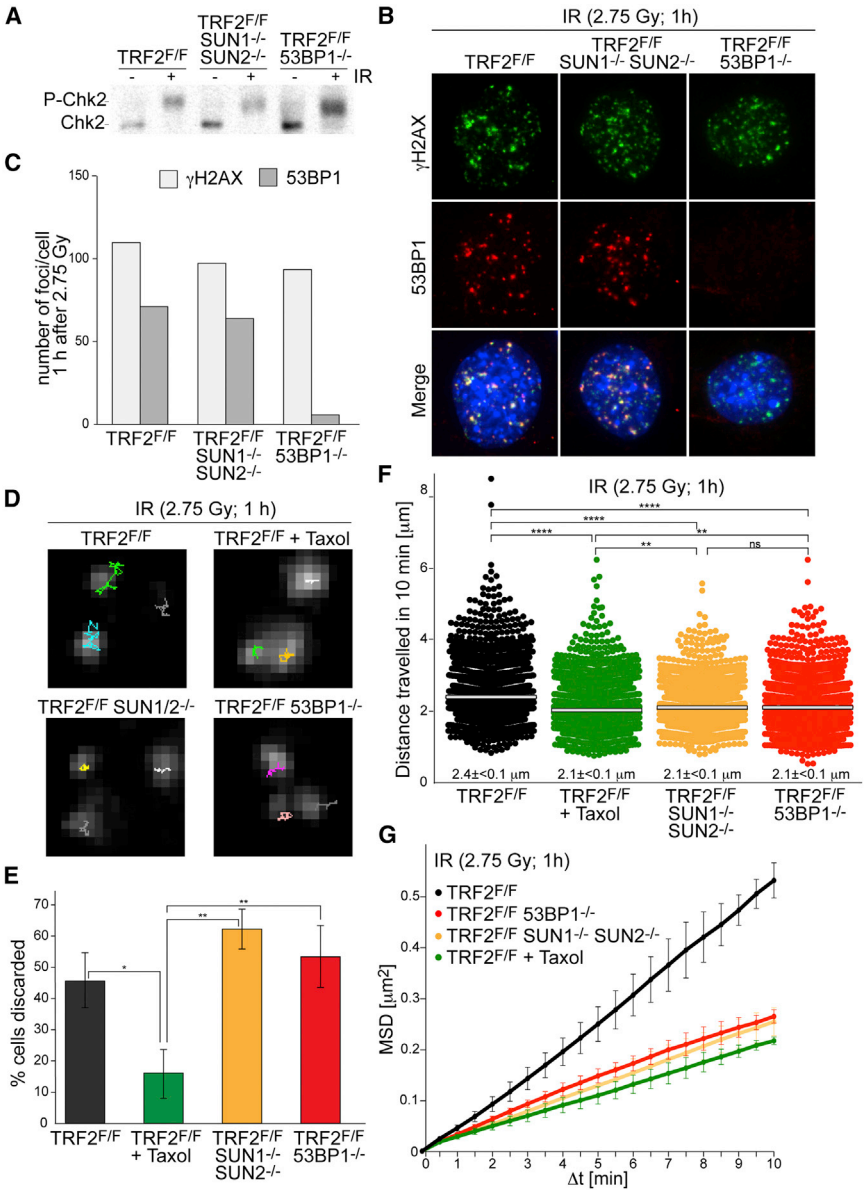

Figure 5. 53BP1/LINC/Microtubule-Promoted Mobility of IR-Induced DSBs

(A) Immunoblot for phosphorylation of Chk2 (as in Figure 2A) in the indicated MEFs at 1 hr after 2.75 Gy IR.

(B) IF for γH2AX (green) and 53BP1 (red) for cells treated as in (A). DAPI, DNA (blue).

(C) Quantification of IR-induced γ-H2AX and 53BP1 foci as assayed in (B).

(D) Examples of 10 min traces of mCherry-53BP1-2 foci at 1 hr after IR of the cells described in (A) with or without 20 μM Taxol (see Movies S5A–S5D).

(E–G) Percentage of cells discarded, distribution of the cumulative distance traveled, and MSDs with SDs of mCherry-BP1-2 foci detected as (D) and (E) (as in Figure 1). Data from three independent experiments.

See also Figure S6 and Table S1.

the telomeres were dysfunctional (Figure S6; Table S1; Movies S6A–S6D). These results indicate that while the chromatin dynamics primarily affects sites of DNA damage, there is also a minor increase in the mobility of undamaged chromatin, consistent with a previous report (Zidovska et al., 2013).

When the eGFP-TRF1 marker was used to detect nuclear deformations, the incidence of distorted nuclei was not affected by deletion of TRF2 (Figure S6B; Table S1), indicating that microtubule dynamics distort nuclei regardless of the presence of DNA damage.

Chromatin Mobility Promotes DSB Mis-repair in BRCA1-Deficient Cells

We considered that for genome-wide DSBs, the increased mobility of the chromatin could promote the joining of unrepaired DNA ends that are at a distance. One setting in which this process may be relevant is the formation of radial chromosomes in PARPi-treated BRCA1-deficient cells. Radial formation involves the joining of a DNA end from one chromosome with a break in another chromosome, which may be at a distance and therefore would require spatial exploration for joining. We therefore tested whether the 53BP1-dependent mobility contributes to the mis-rejoining when many S phase DSBs are induced with PARPi and HDR is impaired. Experiments with cells containing fluorescently labeled geminin to reveal their cell-cycle stage showed that IR-induced DSBs become mobile in S/G2 as well as in G1 (Figures S7A–S7D).

As previously shown, when BRCA1 shRNA-treated cells were incubated with the PARP inhibitor olaparib, a significant number of mis-rejoined chromosomes was formed and this phenotype was repressed by deletion of 53BP1 (Figures 6A–6C). Importantly, SUN1$^{-/-}$SUN2$^{-/-}$ MEFs also diminished the formation of aberrantly repaired chromosomes (Figures 6A–6C) and the mis-rejoining events were strongly reduced by Taxol (Figure 6D). The effect of Taxol was not due to diminished PARP inhibition, since PARPi/Taxol-treated cells showed no parsylation in response to H_2O_2 (Figure S7E). Taxol did not further reduce either the mobility or the chromosome mis-rejoining events in absence of SUN1 and SUN2 (Figures 6E and S7F–S7H; Table S1), supporting the view that the SUN proteins and microtubules act in the same pathway to promote chromatin mobility and aberrant DNA repair. Importantly, SUN1/2 deficiency also diminished the lethality of PARPi treatment in BRCA1-deficient cells (Figures 6F and S7I). As expected, the absence of 53BP1 rescued the lethality of PARPi treatment to a greater extent,

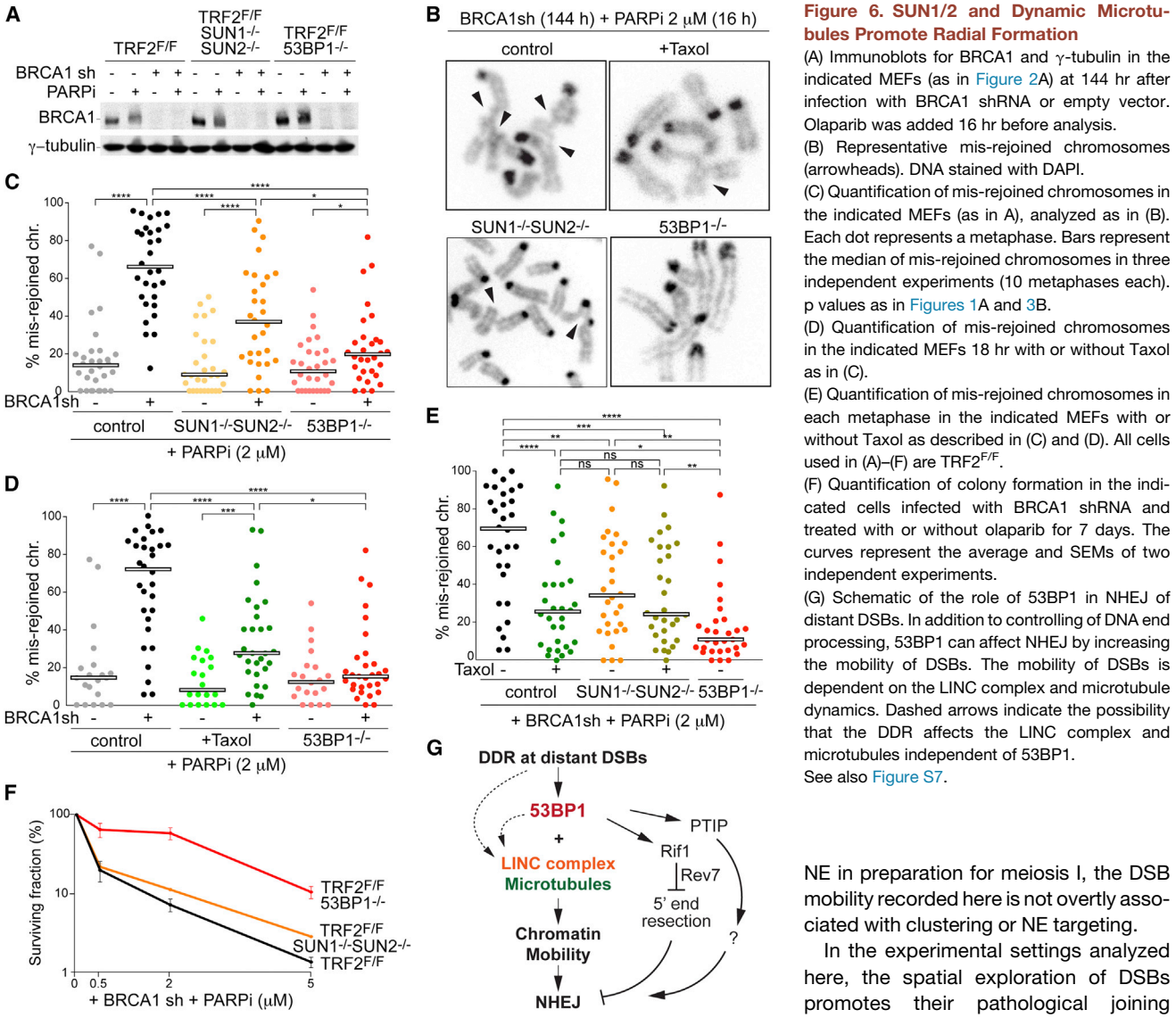

Figure 6. SUN1/2 and Dynamic Microtubules Promote Radial Formation

(A) Immunoblots for BRCA1 and γ-tubulin in the indicated MEFs (as in Figure 2A) at 144 hr after infection with BRCA1 shRNA or empty vector. Olaparib was added 16 hr before analysis.

(B) Representative mis-rejoined chromosomes (arrowheads). DNA stained with DAPI.

(C) Quantification of mis-rejoined chromosomes in the indicated MEFs (as in A), analyzed as in (B). Each dot represents a metaphase. Bars represent the median of mis-rejoined chromosomes in three independent experiments (10 metaphases each). p values as in Figures 1A and 3B.

(D) Quantification of mis-rejoined chromosomes in the indicated MEFs 18 hr with or without Taxol as in (C).

(E) Quantification of mis-rejoined chromosomes in each metaphase in the indicated MEFs with or without Taxol as described in (C) and (D). All cells used in (A)–(F) are TRF2$^{F/F}$.

(F) Quantification of colony formation in the indicated cells infected with BRCA1 shRNA and treated with or without olaparib for 7 days. The curves represent the average and SEMs of two independent experiments.

(G) Schematic of the role of 53BP1 in NHEJ of distant DSBs. In addition to controlling of DNA end processing, 53BP1 can affect NHEJ by increasing the mobility of DSBs. The mobility of DSBs is dependent on the LINC complex and microtubule dynamics. Dashed arrows indicate the possibility that the DDR affects the LINC complex and microtubules independent of 53BP1.

See also Figure S7.

consistent with the multiple mechanisms by which 53BP1 affects DSB repair (Figure 6G).

DISCUSSION

These results establish that DSBs show altered dynamic behavior in mammalian nuclei. The mobility and roaming of damaged chromatin requires the MOB domain in 53BP1, the SUN1/2 components of the LINC complex, and dynamic microtubules. In addition, data on telomere fusions implicated plus-end directed microtubule motors (kinesin-1 and kinesin-2) and at least one of the nesprin proteins in this process. The LINC complex contributes to the dynamic behavior of specific chromosomal loci, including telomeres, during bouquet formation in many eukaryotes (reviewed in Shibuya and Watanabe, 2014). However, the process acting on DSBs is different from bouquet formation. While the bouquet configuration bundles loci at one area of the NE in preparation for meiosis I, the DSB mobility recorded here is not overtly associated with clustering or NE targeting.

In the experimental settings analyzed here, the spatial exploration of DSBs promotes their pathological joining by NHEJ. DSB mobility enhanced telomere-telomere fusions forming dangerous dicentric chromosomes and similarly, it promoted the mis-repair of PARPi-induced DSBs generating lethal radial chromosomes. Given these fatal outcomes, a major question is why this pathway is allowed to act on DSBs. Below, we propose that the enhanced mobility of DSBs represents a mechanism to restore the connection between DNA ends that have lost their proper interaction. We argue that this mechanism can counteract ectopic repair when DSBs are rare, as is the case under physiological conditions. On the other hand, DSB mobility will promote mis-repair under experimental conditions when a high number of DSBs are generated at the same time.

How DSB Mobility Could Prevent Repair Errors in G1 and S/G2

It is reasonable to assume that 53BP1 did not evolve to promote the fusion of dysfunctional telomeres and mis-repair of DSBs in

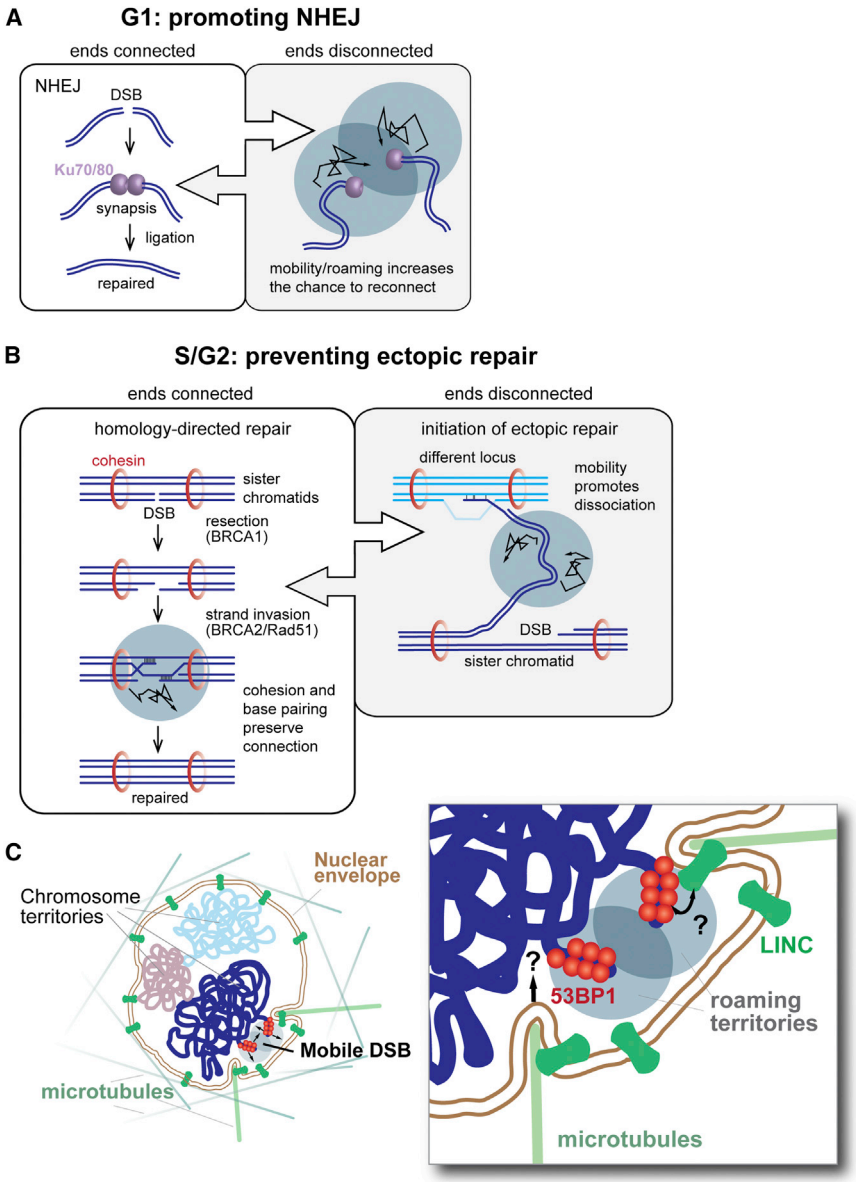

Figure 7. Proposed Function and Mechanism of 53BP1-Dependent Mobility of DSBs

(A and B) Proposed function for 53BP1-dependent mobility in promoting correct DSB repair. (A) G1: mobility of DNA ends that have lost their association could promote their rejoining, thereby promoting NHEJ. (B) S/G2: if a DNA end loses connection with the sister chromatid and invades an ectopic locus, DSB mobility could disrupt this aberrant interaction and promote correct HDR. If the DSB is being repaired correctly using HDR on the sister chromatid, mobility will not dissociate the ends because of the presence of cohesin and base-pairing.

(C) Proposed models for the mechanism of 53BP1/LINC/microtubule-dependent mobility of DSBs. The enlarged part of the nucleus shows 53BP1 (red) at a DSB with the ends separated. One end (top) portrays a model in which 53BP1 has a physical connection with the LINC complex (green). The LINC complex connects to dynamic microtubules and thereby moves the LINC-bound 53BP1-covered DNA end. The other end (bottom) portrays a model in which there is no physical connection between the LINC complex and 53BP1. The LINC complex associates with microtubules that "poke" the nucleus. The 53BP1-associated chromatin moves more readily even when not at the periphery, perhaps because 53BP1 alters the flexibility of the chromatin fiber. See text for discussion.

PARPi-treated BRCA1-deficient cells. Instead, we propose that 53BP1 has gained the ability to promote DSB mobility to facilitate correct repair (Figure 7). We imagine two settings where increased chromatin mobility at a DSB would be advantageous. The first setting is in G1 when a DSB is formed and its repair by Ku70/80-dependent c-NHEJ is the preferred mechanism to re-establish the integrity of the genome (Figure 7A). If Ku loading fails or synapsis does not occur, the DNA ends might become spatially separated. For instance, chromatin-remodeling and nucleosome eviction at DSBs (reviewed in Peterson and Almouzni, 2013) may drive the two DNA ends apart. If the separated ends are mobile, their increased spatial exploration could reconnect them and promote their joining.

The second setting in which mobility of damaged chromatin could prevent repair errors is after DNA replication (Figure 7B). In S/G2, DSBs can be repaired by HDR using the sister chromatid as the template. However, if the DNA topology is unfavorable, one DNA end (or both) could lose its attachment to the sister chromatid and initiate ectopic repair on a different locus (Figure 7B). Mobility of the chromatin near the DSB could help to disconnect the wandering DNA end from an ectopic locus where it is not held down by cohesin and where base-pairing will be limited. In contrast, chromatin mobility of DSBs is less likely to interrupt HDR on the sister because of the stabilizing effects of cohesion and base-pairing.

The proposed role of DSB mobility in counteracting ectopic interactions is analogous to what has been proposed for the mobility of the chromosome pairing centers in *Caenorhabditis elegans* meiosis (Sato et al., 2009). Sato et al. (2009) argued that this process preferentially disrupt pairing of non-homologous chromosomes since paired homologs will have a greater ability to resist forces. Although the system described here is different from the meiotic events, both regulatory pathways may have evolved to provide a mechanism aimed to distinguish weak non-homologous interactions from the stronger connection afforded by homology.

A key consideration with regard to the role of 53BP1 in DSB repair is that the mammalian DDR did not evolve to handle

hundreds of DSBs occurring at the same time. In vivo, the majority of cells in primate brain and liver show no evidence of DSBs and only 10% of the cells have one or two 53BP1 foci (Fumagalli et al., 2012); U. Herbig, personal communication), indicating that the occurrence of multiple DSBs in one nucleus is rare in post-mitotic tissues. Furthermore, in MEFs that are in S phase, where DSBs are expected to be more frequent, <20% of the nuclei have five or more 53BP1 foci and none showed more than ten (Wu et al., 2010). This number of potential S phase DSBs may be an overestimate because 53BP1 foci can form at a variety of DNA lesions. These observations argue that the 53BP1-mediated mobility of DSBs is unlikely to cause chromosomal aberrations unless cells experience an exogenous genotoxic insult.

Models for the Mechanism by Which DSB Mobility Is Generated

We are considering two general types of models for how 53BP1, the LINC complex, and microtubules promote mobility (Figure 7C). In the first model, there is a physical connection between the 53BP1-marked chromatin and a LINC complex that interacts with microtubules. In the second model, no such connection exists.

Although we have not been able to establish a physical interaction between 53BP1 and the SUN proteins, it is not excluded that 53BP1 directs DSBs to the LINC complex. If 53BP1 interacts with the LINC complex, kinesin- and microtubule-dependent mobility of the LINC complex could alter the dynamic behavior of DSBs. The lack of clear peripheral localization of DSBs is not a strong argument against this model since the nuclei we have studied are flat, positioning most of the chromatin fairly close to the NE. Furthermore, NE invaginations could allow a connection of a non-peripheral DSB with the LINC complex. We note that the recorded trajectories and the diffusive behavior of DSBs gleaned from the MSD curves argue against the direct interaction model. However, if the engagement is short-lived and takes place in iterative rapid steps, the outcome may resemble diffusive behavior rather directed movement.

Nonetheless, we favor a second type of model in which no physical connection occurs between 53BP1 and the LINC complex. In this model, the role of the LINC complex is to transduce microtubule forces onto the chromatin in an untargeted manner. This process may be analogous to the microtubule-mediated fenestration of the nuclear envelope in prophase, which is in part mediated by the SUN proteins (Turgay et al., 2014). Random "poking" of the nucleus in response to DNA damage would explain why the global chromatin becomes slightly more dynamic in cells with DSBs but how this process is activated by the DNA damage response remains to be determined. It is also unclear whether the visco-elastic properties of chromatin and the resistance of the lamin network allow force propagation over the required distance.

How could microtubule forces specifically increase the mobility of DNA damaged loci in absence of a connection between 53BP1 and the LINC complex? The simplest explanation would be that 53BP1, through a factor that binds to the MOB domain, changes the flexibility of the chromatin fiber containing the DSB. Increased flexibility of the large chromatin domain containing 53BP1 could render it more sensitive to the microtubule forces transduced through the NE. Indeed, chromatin that contains DSBs shows a decreased density as determined by EM and appears to expand (Kruhlak et al., 2006), attributes that could be consistent with a change in the flexibility of the chromatin fibers.

Implications

This study revealed that mammalian cells use microtubules in the cytoplasm to promote the mobility of sites of DNA damage in the nucleus. Although some of the molecular details of this process remain to be determined, the main players, including the MOB domain of 53BP1, the LINC complex, kinesins, and microtubules are now known, allowing further investigation. The results show that in cells with many DSBs, the induced mobility of the damaged chromatin can promote aberrant DSB repair events, including the fusion of dysfunctional telomeres and formation of radial chromosomes in PARPi-treated BRCA1-deficient cells. Two main issues warrant attention in the near future. First, one prediction from our findings is that curbing microtubule dynamics with taxanes might limit the efficacy of PARPi-treatment of HR-deficient cancers. Thus, when a combination of taxanes with olaparib or other DNA-damaging agents (e.g., platin drugs) is being considered, the effect of taxanes on the efficacy of genotoxic drugs merits further testing. Second, it will be of interest to test our proposal that the 53BP1-dependent mobility of DSBs can prevent DNA repair errors under normal physiological settings when DSBs are rare.

EXPERIMENTAL PROCEDURES

Live-Cell Imaging and Identification of Distorted Nuclei

Dysfunctional telomeres were visualized using mCherry-BP1-2 as described previously (Dimitrova et al., 2008). Images were deconvolved and 2D-maximum intensity projection images were obtained using SoftWoRx software. Tracking of mCherry-BP1-2 foci was performed with ImageJ software on at least ten cells per condition. Cells were registered by the StackReg plugin using Rigid Body (Thévenaz et al., 1998) and particles were tracked using the Mosaic Particle Detector and Tracker plugin (Sbalzarini and Koumoutsakos, 2005) with the following parameters for particle detection and tracking: radius = 1–2 pixels; cutoff = 1–2 pixels; percentile = 6; link range = 1; displacement = 5 pixels. The x and y coordinates of each trajectory were used for further calculation. All mCherry-BP1-2 foci in a cell that were continuously tracked for at least 19 out of 20 frames were analyzed. The analysis of the eGFP-TRF1-marked telomeres was similarly conducted using the following parameters: radius = 1 pixel; cutoff = 1 pixel; percentile = 8–12; link range = 1; displacement = 5 pixels.

The average x and y values of all the foci was calculated in each frame as the geometrical center (GC) and normalized over the $GC_{t=0}$. The distance traveled by the GC between each time points t = b and t = a was calculated as movement of geometrical center

$$MGC_{b-a} = \sqrt{\left(x^{GC}_{t=b} - x^{GC}_{t=a}\right)^2 + \left(y^{GC}_{t=b} - y^{GC}_{t=a}\right)^2},$$

and the maximal MGC (MMGC) for each cell was identified. Cells were discarded if their MMGC exceeded the arbitrary threshold of 2, or if their MMGC exceeded the secondary threshold of 1 and another parameter was also above threshold.

The difference of the average distances of all the *i* foci in the cell and $GC_{t=0}$ (ΔAD) between each time points t = b and t = a was calculated as

$$\Delta AD_{b-a} = \left| \left(\frac{\sum_{i=1}^{n} \sqrt{\left(x^i_{t=b} - x^{GC}_{t=0}\right)^2 + \left(y^i_{t=b} - y^{GC}_{t=0}\right)^2}}{n} \right) - \left(\frac{\sum_{i=1}^{n} \sqrt{\left(x^i_{t=a} - x^{GC}_{t=0}\right)^2 + \left(y^i_{t=a} - y^{GC}_{t=0}\right)^2}}{n} \right) \right|,$$

and the maximal ΔAD (MΔAD) for each cell was identified. Cells were discarded if MΔAD exceeded the arbitrary threshold of 2, or if MΔAD exceeded the secondary threshold of 1 and another parameter was also above threshold.

Finally, the trajectories traveled by each focus *i* per cell, relatively to the GC, were normalized to the coordinates $x^i_{t=0}$ and $y^i_{t=0}$ and projected together on a XY plane. The percentage of foci in each quadrant was calculated for each time frame: upper right (UR(%)), lower right (LR(%)), upper left (UL(%)), lower left (LL(%)) and the average of these values during the time lapse was derived. Laterality (LAT (%)), verticality (VER (%)), and diagonality (DIA (%)) were calculated for each time frame as:

$$LAT(\%) = |(((UR(\%) + LR(\%)) \div 100) - 0.5) \div 0.5| \times 100,$$

$$VER(\%) = |(((UR(\%) + UL(\%)) \div 100) - 0.5) \div 0.5| \times 100,$$

$$DIA(\%) = |(((UR(\%) + LL(\%)) \div 100) - 0.5) \div 0.5| \times 100,$$

and the average of these values during the time lapse were derived. Cells were discarded if UR, LR, UL, LL, LAT, VER, or DIA exceeded the arbitrary threshold of 40%, or if they exceeded the secondary threshold of 30% and another parameter was also above threshold.

the Cumulative Distance traveled in 10 min by each of the foci *i* (CD^i) was calculated relative to the GC, as previously described (Dimitrova et al., 2008), as

$$CD^i = \sum_{t=1}^{20} \sqrt{\left((x^t_i - x^{GC}_t) - (x^i_{t-1} - x^{GC}_{t-1})\right)^2 + \left((y^i_t - y^{GC}_t) - (y^i_{t-1} - y^{GC}_{t-1})\right)^2}.$$

Mean square displacement (MSD) was calculated as

$$MSD(\Delta t) = \frac{1}{n} \times \sum_{i=1}^{n} D_i(\Delta t)^2,$$

where

$$D_i(\Delta t) = \sqrt{\left((x^i_t - x^{GC}_t) - (x^i_{t-\Delta t} - x^{GC}_{t-\Delta t})\right)^2 + \left((y^i_t - y^{GC}_t) - (y^i_{t-\Delta t} - y^{GC}_{t-\Delta t})\right)^2}.$$

All data output in pixels (standard ImageJ output) were converted to meters by the formula, 1 pixel = 0.215 μm, based on the characteristics of the objective.

Diffusion coefficient D was calculated as

$$D = m/4,$$

where *m* is the slope of the MSD after fitting to a linear curve. The anomalous diffusion coefficient α was derived using MATLAB by the fitting of MSD to the diffusion model function:

$$MSD = A + \Gamma t^{\alpha}.$$

For cumulative distance, statistical analysis was performed using Prism Software applying the Mann-Whitney test.

Other Experimental Procedures

All procedures for derivation of MEFs, cell treatments, plasmids, shRNAs, immunoblotting, IF, IF-FISH, analysis of metaphase chromosomes, in-gel analysis of telomeric DNA, co-immunoprecipitation, ChIP, and mutagenesis were performed using previously published standard procedures. The mutated 53BP1 alleles were as follows: 53BP1ΔPTIP (S6A, S13A, S25A, S29A) and 53BP1ΔMOB (S674A, T696A, S698A, S784A, S831A, T855A, S892A, S1068A, S1086A, S1104A, T1148A, S1171A, S1219A).

Detailed experimental procedures are given in the Supplemental Experimental Procedures.

SUPPLEMENTAL INFORMATION

Supplemental Information includes Supplemental Experimental Procedures, seven figures, one table, and six movies and can be found with this article online at http://dx.doi.org/10.1016/j.cell.2015.09.057.

AUTHOR CONTRIBUTIONS

R.A.K. performed the experiments on the 53BP1 mutants and the ChIP in Figure S2A. F.L. did all other experiments. N.D. discovered the effect of Nocodazole on the mobility of dysfunctional telomeres. T.d.L. designed experiments and wrote the paper with F.L.

ACKNOWLEDGMENTS

We are deeply grateful to Devon White for his expert mouse husbandry. We are grateful to Dr. Andrea Panza for help in developing the automated image analysis, Alejandro Dottore for help with MSD analysis, and Dr. Franco Flandoli for helpful discussion. We thank members of the T.d.L. lab for discussion and help with this manuscript. We thank Drs. G. Hannon, D. Livingston, and P. Igarashi and L.S.W. Goldstein for reagents and Drs. T. Kapoor and S. Gasser for discussion. A. North (RU Bio-imaging Core Facility) is thanked for assistance with DeltaVision microscopy. F.L. was supported by a Rockefeller University Women and Science postdoctoral fellowship. R.K. is the recipient of a Boehringer Ingleheim Fonds graduate fellowship. This work was supported by grants from the NCI (5R01CA181090) and the Breast Cancer Research Foundation. T.d.L. is an American Cancer Society Research Professor.

Received: July 7, 2015
Revised: September 14, 2015
Accepted: September 28, 2015
Published: November 5, 2015

REFERENCES

Agmon, N., Liefshitz, B., Zimmer, C., Fabre, E., and Kupiec, M. (2013). Effect of nuclear architecture on the efficiency of double-strand break repair. Nat. Cell Biol. *15*, 694–699.

Aten, J.A., Stap, J., Krawczyk, P.M., van Oven, C.H., Hoebe, R.A., Essers, J., and Kanaar, R. (2004). Dynamics of DNA double-strand breaks revealed by clustering of damaged chromosome domains. Science *303*, 92–95.

Banerjee, S., Kaye, S.B., and Ashworth, A. (2010). Making the best of PARP inhibitors in ovarian cancer. Nat. Rev. Clin. Oncol. *7*, 508–519.

Becker, A., Durante, M., Taucher-Scholz, G., and Jakob, B. (2014). ATM alters the otherwise robust chromatin mobility at sites of DNA double-strand breaks (DSBs) in human cells. PLoS ONE *9*, e92640.

Boersma, V., Moatti, N., Segura-Bayona, S., Peuscher, M.H., van der Torre, J., Wevers, B.A., Orthwein, A., Durocher, D., and Jacobs, J.J. (2015). MAD2L2 controls DNA repair at telomeres and DNA breaks by inhibiting 5′ end resection. Nature *521*, 537–540.

Bothmer, A., Robbiani, D.F., Di Virgilio, M., Bunting, S.F., Klein, I.A., Feldhahn, N., Barlow, J., Chen, H.T., Bosque, D., Callen, E., et al. (2011). Regulation of DNA end joining, resection, and immunoglobulin class switch recombination by 53BP1. Mol. Cell *42*, 319–329.

Bouwman, P., Aly, A., Escandell, J.M., Pieterse, M., Bartkova, J., van der Gulden, H., Hiddingh, S., Thanasoula, M., Kulkarni, A., Yang, Q., et al. (2010). 53BP1 loss rescues BRCA1 deficiency and is associated with triple-negative and BRCA-mutated breast cancers. Nat. Struct. Mol. Biol. *17*, 688–695.

Bunting, S.F., Callén, E., Wong, N., Chen, H.T., Polato, F., Gunn, A., Bothmer, A., Feldhahn, N., Fernandez-Capetillo, O., Cao, L., et al. (2010). 53BP1 inhibits homologous recombination in Brca1-deficient cells by blocking resection of DNA breaks. Cell *141*, 243–254.

Callen, E., Di Virgilio, M., Kruhlak, M.J., Nieto-Soler, M., Wong, N., Chen, H.T., Faryabi, R.B., Polato, F., Santos, M., Starnes, L.M., et al. (2013). 53BP1 mediates productive and mutagenic DNA repair through distinct phosphoprotein interactions. Cell *153*, 1266–1280.

Cao, L., Xu, X., Bunting, S.F., Liu, J., Wang, R.H., Cao, L.L., Wu, J.J., Peng, T.N., Chen, J., Nussenzweig, A., et al. (2009). A selective requirement for 53BP1 in the biological response to genomic instability induced by Brca1 deficiency. Mol. Cell *35*, 534–541.

Chang, W., Worman, H.J., and Gundersen, G.G. (2015). Accessorizing and anchoring the LINC complex for multifunctionality. J. Cell Biol. *208*, 11–22.

Chapman, J.R., Barral, P., Vannier, J.B., Borel, V., Steger, M., Tomas-Loba, A., Sartori, A.A., Adams, I.R., Batista, F.D., and Boulton, S.J. (2013). RIF1 is essential for 53BP1-dependent nonhomologous end joining and suppression of DNA double-strand break resection. Mol. Cell *49*, 858–871.

Chen, B., Gilbert, L.A., Cimini, B.A., Schnitzbauer, J., Zhang, W., Li, G.W., Park, J., Blackburn, E.H., Weissman, J.S., Qi, L.S., and Huang, B. (2013). Dynamic imaging of genomic loci in living human cells by an optimized CRISPR/Cas system. Cell *155*, 1479–1491.

Cho, N.W., Dilley, R.L., Lampson, M.A., and Greenberg, R.A. (2014). Interchromosomal homology searches drive directional ALT telomere movement and synapsis. Cell *159*, 108–121.

Crisp, M., Liu, Q., Roux, K., Rattner, J.B., Shanahan, C., Burke, B., Stahl, P.D., and Hodzic, D. (2006). Coupling of the nucleus and cytoplasm: role of the LINC complex. J. Cell Biol. *172*, 41–53.

Di Virgilio, M., Callen, E., Yamane, A., Zhang, W., Jankovic, M., Gitlin, A.D., Feldhahn, N., Resch, W., Oliveira, T.Y., Chait, B.T., et al. (2013). Rif1 prevents resection of DNA breaks and promotes immunoglobulin class switching. Science *339*, 711–715.

Dimitrova, N., Chen, Y.C., Spector, D.L., and de Lange, T. (2008). 53BP1 promotes non-homologous end joining of telomeres by increasing chromatin mobility. Nature *456*, 524–528.

Ding, X., Xu, R., Yu, J., Xu, T., Zhuang, Y., and Han, M. (2007). SUN1 is required for telomere attachment to nuclear envelope and gametogenesis in mice. Dev. Cell *12*, 863–872.

Dion, V., and Gasser, S.M. (2013). Chromatin movement in the maintenance of genome stability. Cell *152*, 1355–1364.

Dion, V., Kalck, V., Horigome, C., Towbin, B.D., and Gasser, S.M. (2012). Increased mobility of double-strand breaks requires Mec1, Rad9 and the homologous recombination machinery. Nat. Cell Biol. *14*, 502–509.

Escribano-Díaz, C., Orthwein, A., Fradet-Turcotte, A., Xing, M., Young, J.T., Tkáč, J., Cook, M.A., Rosebrock, A.P., Munro, M., Canny, M.D., et al. (2013). A cell cycle-dependent regulatory circuit composed of 53BP1-RIF1 and BRCA1-CtIP controls DNA repair pathway choice. Mol. Cell *49*, 872–883.

Falk, M., Lukasova, E., Gabrielova, B., Ondrej, V., and Kozubek, S. (2007). Chromatin dynamics during DSB repair. Biochim. Biophys. Acta *1773*, 1534–1545.

Feng, L., Fong, K.W., Wang, J., Wang, W., and Chen, J. (2013). RIF1 counteracts BRCA1-mediated end resection during DNA repair. J. Biol. Chem. *288*, 11135–11143.

Fumagalli, M., Rossiello, F., Clerici, M., Barozzi, S., Cittaro, D., Kaplunov, J.M., Bucci, G., Dobreva, M., Matti, V., Beausejour, C.M., et al. (2012). Telomeric DNA damage is irreparable and causes persistent DNA-damage-response activation. Nat. Cell Biol. *14*, 355–365.

Gandhi, M., Evdokimova, V.N.T., T Cuenco, K., Nikiforova, M.N., Kelly, L.M., Stringer, J.R., Bakkenist, C.J., and Nikiforov, Y.E. (2012). Homologous chromosomes make contact at the sites of double-strand breaks in genes in somatic G0/G1-phase human cells. Proc. Natl. Acad. Sci. USA *109*, 9454–9459.

Jakob, B., Splinter, J., and Taucher-Scholz, G. (2009). Positional stability of damaged chromatin domains along radiation tracks in mammalian cells. Radiat. Res. *171*, 405–418.

Ketema, M., Wilhelmsen, K., Kuikman, I., Janssen, H., Hodzic, D., and Sonnenberg, A. (2007). Requirements for the localization of nesprin-3 at the nuclear envelope and its interaction with plectin. J. Cell Sci. *120*, 3384–3394.

Kruhlak, M.J., Celeste, A., Dellaire, G., Fernandez-Capetillo, O., Müller, W.G., McNally, J.G., Bazett-Jones, D.P., and Nussenzweig, A. (2006). Changes in chromatin structure and mobility in living cells at sites of DNA double-strand breaks. J. Cell Biol. *172*, 823–834.

Lei, K., Zhang, X., Ding, X., Guo, X., Chen, M., Zhu, B., Xu, T., Zhuang, Y., Xu, R., and Han, M. (2009). SUN1 and SUN2 play critical but partially redundant roles in anchoring nuclei in skeletal muscle cells in mice. Proc. Natl. Acad. Sci. USA *106*, 10207–10212.

Lottersberger, F., Bothmer, A., Robbiani, D.F., Nussenzweig, M.C., and de Lange, T. (2013). Role of 53BP1 oligomerization in regulating double-strand break repair. Proc. Natl. Acad. Sci. USA *110*, 2146–2151.

Mahen, R., Hattori, H., Lee, M., Sharma, P., Jeyasekharan, A.D., and Venkitaraman, A.R. (2013). A-type lamins maintain the positional stability of DNA damage repair foci in mammalian nuclei. PLoS ONE *8*, e61893.

Miné-Hattab, J., and Rothstein, R. (2012). Increased chromosome mobility facilitates homology search during recombination. Nat. Cell Biol. *14*, 510–517.

Munoz, I.M., Jowsey, P.A., Toth, R., and Rouse, J. (2007). Phospho-epitope binding by the BRCT domains of hPTIP controls multiple aspects of the cellular response to DNA damage. Nucleic Acids Res. *35*, 5312–5322.

Neumaier, T., Swenson, J., Pham, C., Polyzos, A., Lo, A.T., Yang, P., Dyball, J., Asaithamby, A., Chen, D.J., Bissell, M.J., et al. (2012). Evidence for formation of DNA repair centers and dose-response nonlinearity in human cells. Proc. Natl. Acad. Sci. USA *109*, 443–448.

Padmakumar, V.C., Libotte, T., Lu, W., Zaim, H., Abraham, S., Noegel, A.A., Gotzmann, J., Foisner, R., and Karakesisoglou, I. (2005). The inner nuclear membrane protein Sun1 mediates the anchorage of Nesprin-2 to the nuclear envelope. J. Cell Sci. *118*, 3419–3430.

Palm, W., and de Lange, T. (2008). How shelterin protects mammalian telomeres. Annu. Rev. Genet. *42*, 301–334.

Panier, S., and Boulton, S.J. (2014). Double-strand break repair: 53BP1 comes into focus. Nat. Rev. Mol. Cell Biol. *15*, 7–18.

Peterson, C.L., and Almouzni, G. (2013). Nucleosome dynamics as modular systems that integrate DNA damage and repair. Cold Spring Harb. Perspect. Biol. *5*, a012658.

Rothkamm, K., and Löbrich, M. (2003). Evidence for a lack of DNA double-strand break repair in human cells exposed to very low x-ray doses. Proc. Natl. Acad. Sci. USA *100*, 5057–5062.

Roux, K.J., Crisp, M.L., Liu, Q., Kim, D., Kozlov, S., Stewart, C.L., and Burke, B. (2009). Nesprin 4 is an outer nuclear membrane protein that can induce kinesin-mediated cell polarization. Proc. Natl. Acad. Sci. USA *106*, 2194–2199.

Sato, A., Isaac, B., Phillips, C.M., Rillo, R., Carlton, P.M., Wynne, D.J., Kasad, R.A., and Dernburg, A.F. (2009). Cytoskeletal forces span the nuclear envelope to coordinate meiotic chromosome pairing and synapsis. Cell *139*, 907–919.

Sbalzarini, I.F., and Koumoutsakos, P. (2005). Feature point tracking and trajectory analysis for video imaging in cell biology. J. Struct. Biol. *151*, 182–195.

Seeber, A., Dion, V., and Gasser, S.M. (2013). Checkpoint kinases and the INO80 nucleosome remodeling complex enhance global chromatin mobility in response to DNA damage. Genes Dev. *27*, 1999–2008.

Shibuya, H., and Watanabe, Y. (2014). The meiosis-specific modification of mammalian telomeres. Cell Cycle *13*, 2024–2028.

Soutoglou, E., Dorn, J.F., Sengupta, K., Jasin, M., Nussenzweig, A., Ried, T., Danuser, G., and Misteli, T. (2007). Positional stability of single double-strand breaks in mammalian cells. Nat. Cell Biol. *9*, 675–682.

Starr, D.A., and Fridolfsson, H.N. (2010). Interactions between nuclei and the cytoskeleton are mediated by SUN-KASH nuclear-envelope bridges. Annu. Rev. Cell Dev. Biol. *26*, 421–444.

Swartz, R.K., Rodriguez, E.C., and King, M.C. (2014). A role for nuclear envelope-bridging complexes in homology-directed repair. Mol. Biol. Cell *25*, 2461–2471.

Thévenaz, P., Ruttimann, U.E., and Unser, M. (1998). A pyramid approach to subpixel registration based on intensity. IEEE Trans. Image Process. *7*, 27–41.

Turgay, Y., Champion, L., Balazs, C., Held, M., Toso, A., Gerlich, D.W., Meraldi, P., and Kutay, U. (2014). SUN proteins facilitate the removal of membranes from chromatin during nuclear envelope breakdown. J. Cell Biol. *204*, 1099–1109.

Wang, T., Wei, J.J., Sabatini, D.M., and Lander, E.S. (2014). Genetic screens in human cells using the CRISPR-Cas9 system. Science *343*, 80–84.

Wilson, K.L., and Foisner, R. (2010). Lamin-binding Proteins. Cold Spring Harb. Perspect. Biol. *2*, a000554.

Wu, P., van Overbeek, M., Rooney, S., and de Lange, T. (2010). Apollo contributes to G overhang maintenance and protects leading-end telomeres. Mol. Cell *39*, 606–617.

Xu, G., Chapman, J.R., Brandsma, I., Yuan, J., Mistrik, M., Bouwman, P., Bartkova, J., Gogola, E., Warmerdam, D., Barazas, M., et al. (2015). REV7 counteracts DNA double-strand break resection and affects PARP inhibition. Nature *521*, 541–544.

Zidovska, A., Weitz, D.A., and Mitchison, T.J. (2013). Micron-scale coherence in interphase chromatin dynamics. Proc. Natl. Acad. Sci. USA *110*, 15555–15560.

Zimmermann, M., and de Lange, T. (2014). 53BP1: pro choice in DNA repair. Trends Cell Biol. *24*, 108–117.

Zimmermann, M., Lottersberger, F., Buonomo, S.B., Sfeir, A., and de Lange, T. (2013). 53BP1 regulates DSB repair using Rif1 to control 5′ end resection. Science *339*, 700–704.

Cell

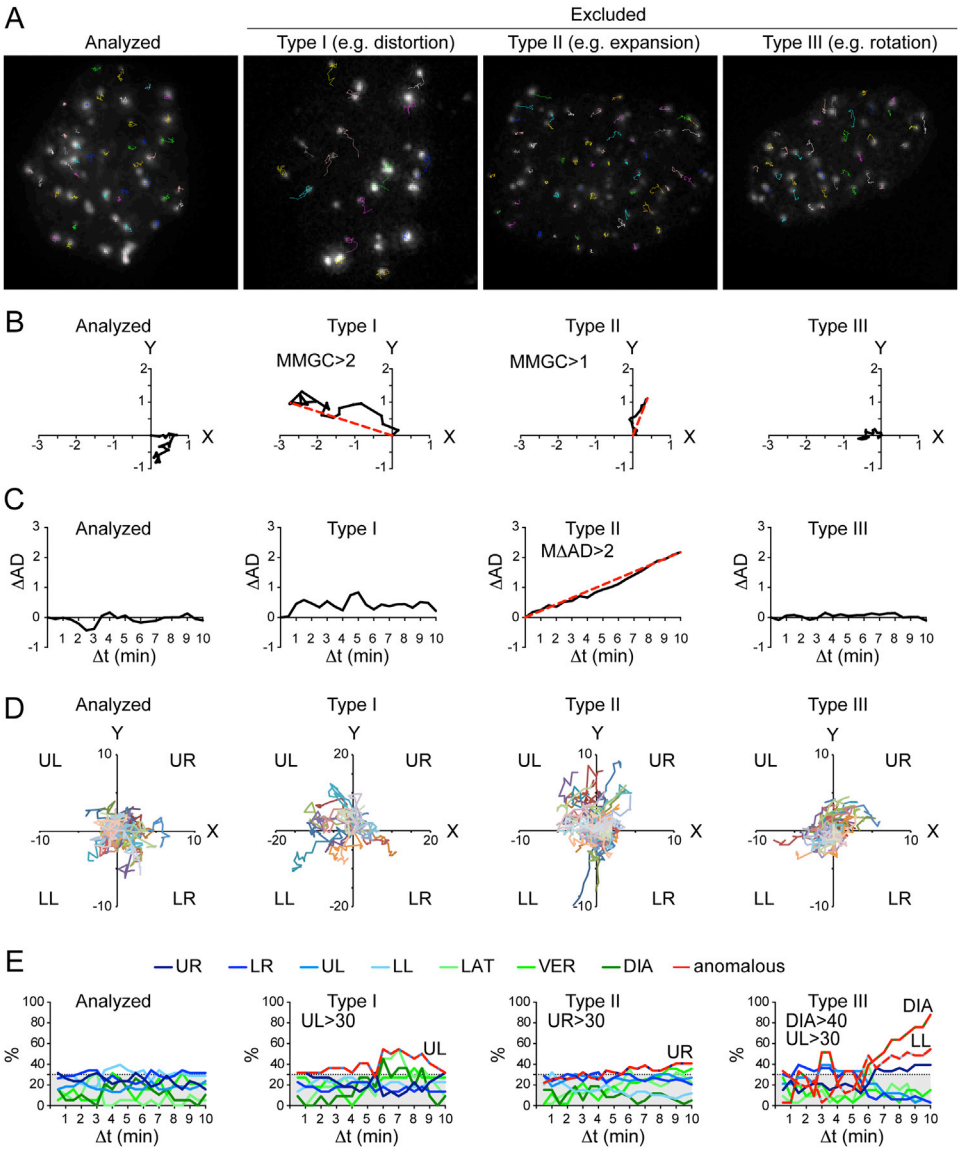

Figure S1. Identification of Distorted Nuclei, Related to Figure 1 and Experimental Procedures

(A) Examples of traces of mCherry-53Bp1-2 foci in SV40LT TRF2$^{F/F}$ RsCre-ER^{T1} MEFs 55-72 hr after TRF2 deletion (see Movies S1A and S2A–S2C). Four nuclei are shown, one of which is considered retaining its shape (analyzed). The other three nuclei represent the three major types of distortions observed.

(B) Movement of the Geometrical Center (MGC) in arbitrary units (a.u.) during the 10 min of imaging in the indicated cells. At time = 0 the coordinates of the Geometrical Center are normalized to (x = 0, y = 0). The dashed red lines indicate when the Maximal MGC (MMGC) $\geq$ 1.

(C) Difference between the Average Distances of the foci from the Geometrical Center at t = 0 (ΔAD) in arbitrary units (a.u.) at the indicated time points in the indicated cells. The dashed red line indicates when the Maximal ΔAD (MΔAD) $\geq$ 1.

(D) Trajectories of all the mCherry53BP1-2 foci in the indicated cells, as if they originated from the same point, in arbitrary units (a.u.). The different colors are randomly assigned to the different trajectories. Note that Type I graph is scaled 1:4.

(E) Graph of the percentage (%) of mCherry-53BP1-2 foci in the quadrants UR, LR, UL, LL and in the combination of two of them (LAT, VER, DIA) as indicated in the legend and described in the text. The dotted black line and the gray background indicate the threshold of 30%. The red lines highlight parameters that are on average above 30%.

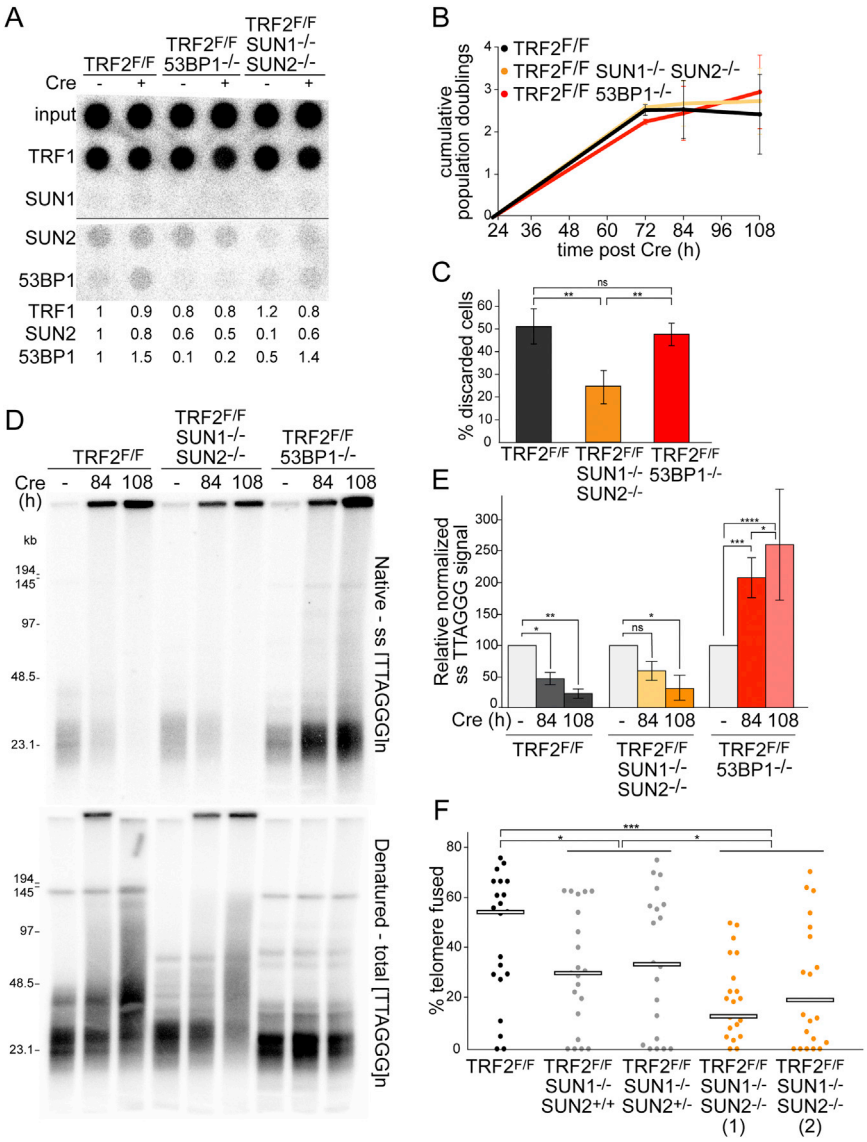

Figure S2. Effects of SUN1/2 on Cell Growth and NHEJ of Dysfunctional Telomeres, Related to Figures 2 and 3

(A) Telomere ChIP performed in the indicated MEFs at 72 hr after Hit&Run Cre with the indicated antibodies. The signals of the telomere DNA recovered with the indicated antibody were normalized to the input and are given relative to the signal in untreated TRF2$^{F/F}$ cells. The SUN1 antibodies did not result in a ChIP signal.

(B) Growth curves. Means of three independent experiment and SDs of cumulative population doublings after Hit&Run Cre (t = 0) of the indicated MEFs used in Figures 2A–2C, 3A, and 3B.

(C) Percentage of MEFs discarded from analysis as in Figures 2D–2F.

(D and E) Detection and quantification of the single-stranded telomere signal and total telomere DNA in the indicated MEFs. Values represent means from four independent experiments with SDs. See Figures 3C and 3D.

(F) Quantification of telomere fusions in the indicated MEFs 96 hr after TRF2 deletion with Hit&Run Cre. Bars represent the median telomere fusions in 20 metaphases in one representative experiment. t test was performed combining the cell lines as indicated.

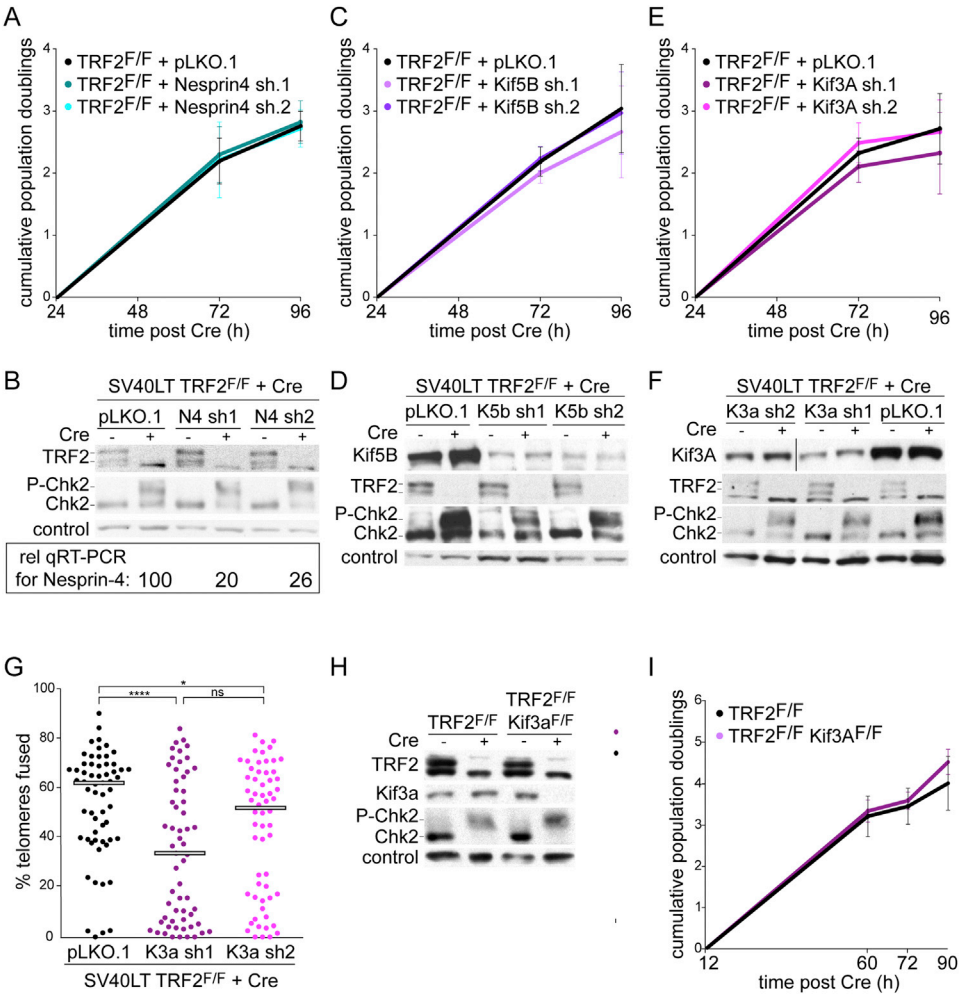

Figure S3. Assays for TRF2 Deletion, Cell Growth, and Telomere Fusions on Depletion of Nesprin-4, Kif3A, and Kif5B, Related to Figure 3

(A–F) Proliferation assays (A, C, E), immunoblots (B, D, F) for TRF2, phosphorylated Chk2 and the indicated kinesins, at 72 hr after TRF2 deletion with Hit&Run Cre in SV40LT-immortalized TRF2$^{F/F}$ MEFs treated with shRNAs to Nesprin-4, Kif5B or Kif3A. Box below (B) shows the relative Nesprin-4 mRNA levels determined by RT-PCR. Graphs represents the means and SDs of three experiments shown in Figures 3F and 3G.

(G) Quantification of telomere fusions in the indicated MEFs. Bars represent the median % of telomeres fused for three independent experiments (20 metaphases each).

(H) Immunoblots for TRF2, Kif3A, and phosphorylated Chk2 at 60 hr after TRF2 deletion from the indicated MEFs used in Figure 3H.

(I) Proliferation assays for the indicated MEFs used in Figure 3H. Graph represents the means and SDs of three independent experiments.

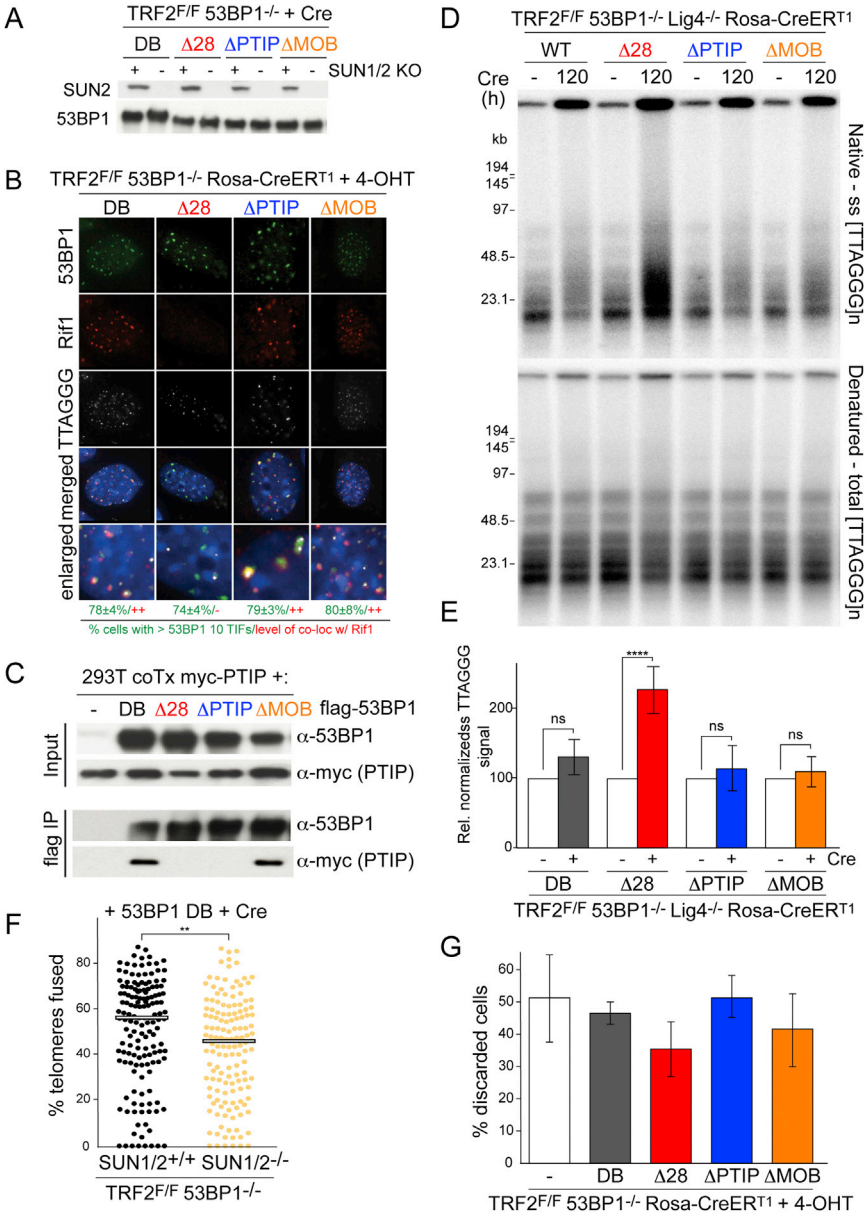

Figure S4. 53BP1ΔMOB Interacts with PTIP and Blocks Resection, Related to Figure 4

(A) Immunoblots for the 53BP1 alleles and SUN2 in the indicated MEFs 72 hr after TRF2 deletion with Hit&Run Cre (see Figures 4A and 4B).

(B) TIF assay on SV40LT TRF2$^{F/F}$ 53BP1$^{-/-}$ RsCre-ER^{T1} MEFs expressing the indicated 53BP1 alleles 72 hr after TRF2 deletion. IF for human 53BP1 (green) and Rif1 (red) combined with telomeric FISH (gray). DAPI: DNA (blue). Numbers below the photographs: averages with SDs of nuclei with ≥ 10 53BP1 TIFs in three independent experiments, scored as in Figures 2B and 2C. The level of colocalization of Rif1 with 53BP1 is indicated in red: complete (++) or absent (-).

(C) Co-IP of PTIP and 53BP1 mutants performed with flag antibody on 293T cells transiently co-trasfected with myc-tagged PTIP and with the indicated flag-tagged 53BP1 alleles. Input (upper panels) and IP (lower panels) were analyzed by immunoblotting for human 53BP1 (first panel) and myc (second panel).

(D and E) Detection and quantification of the single-stranded overhang telomere signal in SV40-immortalized TRF2$^{F/F}$ Lig4$^{-/-}$ 53BP1$^{-/-}$ RsCre-ER^{T1} MEFs expressing the indicated 53BP1 alleles 96 hr after TRF2 deletion. Values represent means for three independent experiments with SDs. Method as in Figure 3.

(F) Quantification of telomere fusions in the indicated MEFs 96 hs after Hit&Run Cre-dependent TRF2 deletion. Each dot represents a metaphase. Bars represent the median of more than 70 metaphases analyzed (in four independent experiments).

(G) Means of three independent experiments with SDs of the percentage of the indicated MEFs discarded from the analysis in the experiment shown in Figure 4C. Using unpaired t test, there was no significant difference between the different cell lines.

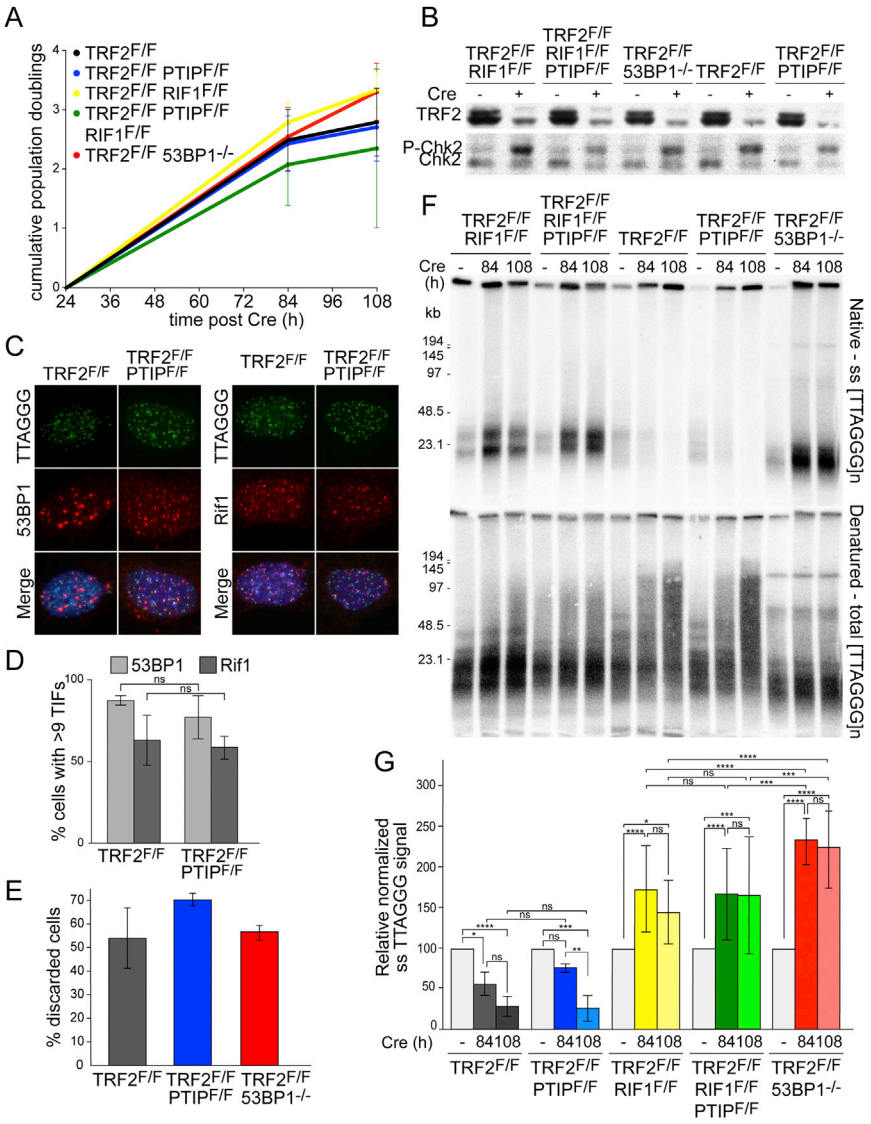

Figure S5. PTIP Does Not Affect Cell Growth or Resection after TRF2 Deletion, Related to Figure 4

(A) Proliferation of the indicated MEFs after Hit&Run Cre (t = 0). Graph represents the means and SDs of five independent experiments.

(B) Immunoblot for TRF2 and phosphorylation of Chk2 in the indicated MEFs as in (A) at 72 hr after TRF2 deletion with Hit&Run Cre.

(C and D) TIF assay on the indicated MEFs 72 hr after Cre. See Figure 2 for details. There is no significant difference between $TRF2^{F/F}$ and $TRF2^{F/F}$ $PTIP^{F/F}$ MEFs using unpaired t test in three independent experiments.

(E) Percentage of the indicated MEFs discarded from analysis in the experiments shown in Figures 4D–4F. Means and SEMs for two independent experiments.

(F and G) Detection and quantification of the single-stranded overhang telomere signal in the indicated MEFs as in (A) at 84 and 108 hr after TRF2 deletion. See Figure 3 for details. Values represent means from five independent experiments with SDs.

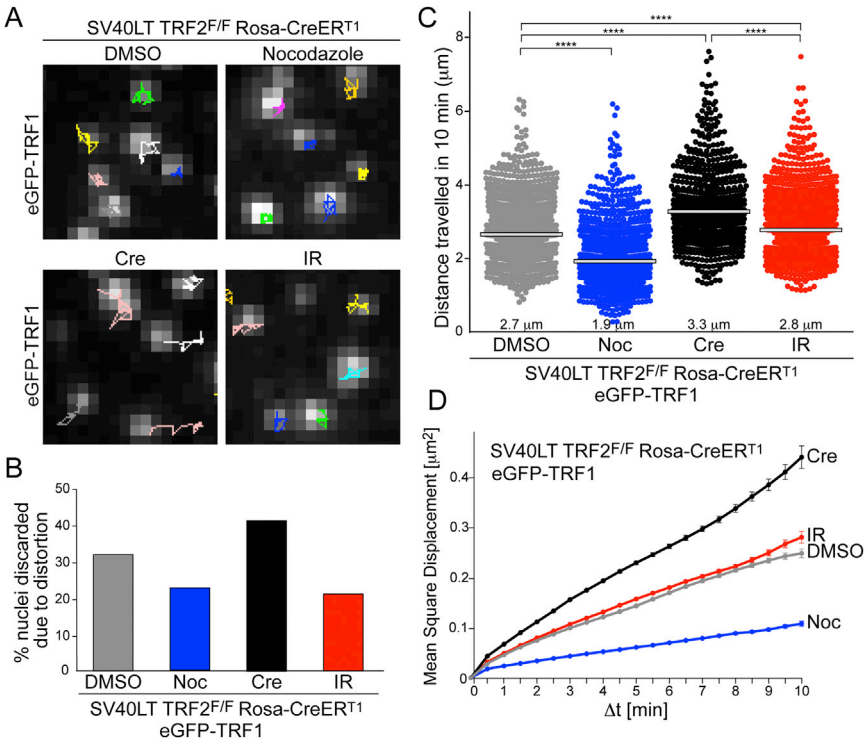

Figure S6. Genome-wide DNA Damage Does Not Alter Nuclear Deformation and Has a Slight Effect on the Mobility of Functional Telomeres, Related to Figure 5

(A) Examples of traces of eGFP-TRF1 foci in SV40LT TRF2$^{F/F}$ RsCre-ER^{T1} MEFs in presence of TRF2, with or without Nocodazole (1 μg/ml), 55-72 hr after TRF2 deletion or 1 hr after 2.75 Gy IR (see Movies S6A–S6D).

(B) Percentage of the cells discarded from further imaging in a representative experiment.

(C and D) Quantification of the cumulative distance traveled (C) and MSD and SEMs (D) of all the eGFP-TRF1 foci detected in the cells in (A) and (B). At least 10 cells and > 500 foci per condition were analyzed. p values as in Figure 1.

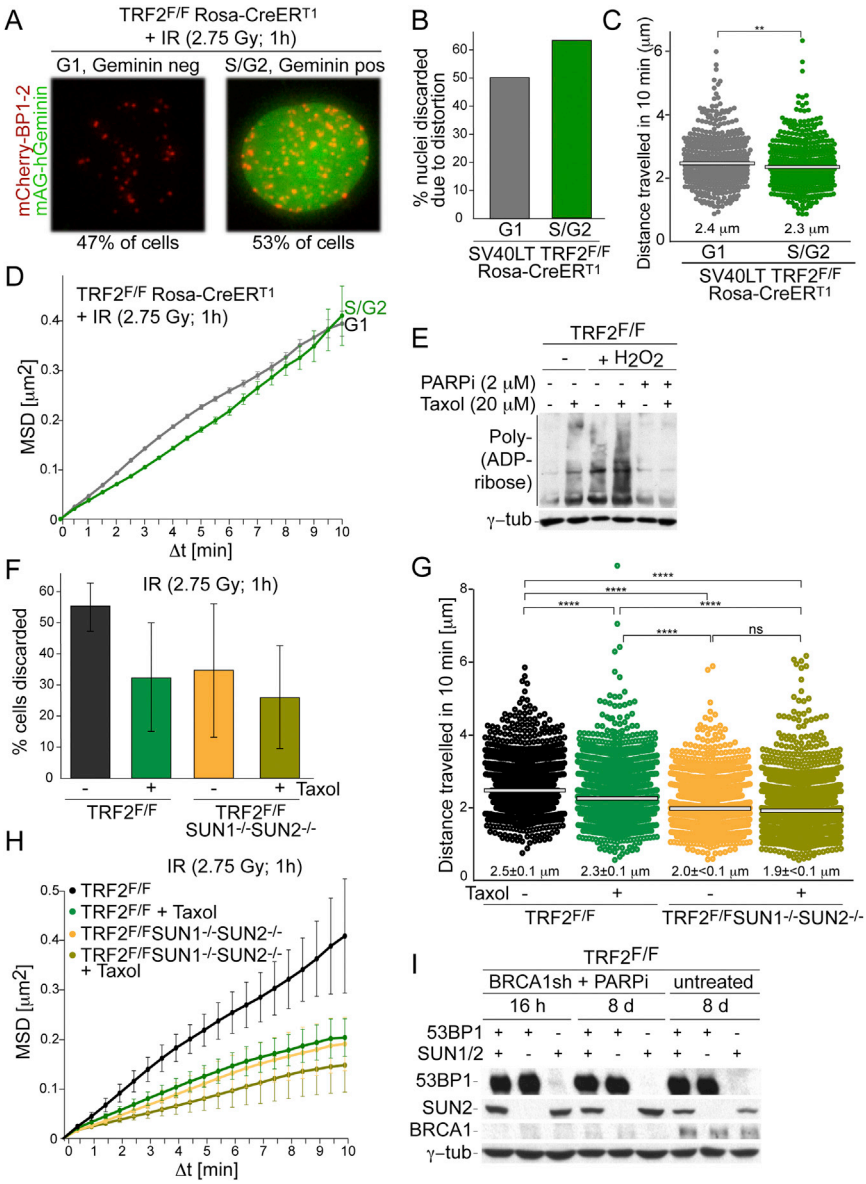

Figure S7. Mobility of IR-Induced DSBs Is Not Affected by the Cell-Cycle Stage and Depends on SUN Proteins, Related to Figure 6

(A) Representative images of cells in G1 (left) or S/G2 (right) based on the mAG-hGeminin (green) cell-cycle marker.

(B–D) Percentage of cells discarded (B), distribution of the cumulative distance traveled (C), and MSDs with SEMs (D) of mCherry-BP1-2 foci detected as (A) in one representative experiments.

(E) Immunoblots for Poly-(ADPribose) and γ-tubulin in MEFs treated with or without H_2O_2 treatment (0.015%, 20 min) with the addition of PARPi (16 h), and Taxol (18 h) as indicated.

(F–H) Percentage of cells discarded (F), distribution of the cumulative distance traveled (G), and MSDs of mCherry-BP1-2 foci (H) detected in the indicated MEFs with or without 20 μM Taxol, at 1 hr after 2.75 Gy IR. Graphs represents the average with SD of three independent experiments. See Figure 1 for technical details.

(I) Immunoblots for 53BP1, SUN2, BRCA1 and γ-tubulin in the indicated MEFs (as in Figure 6F) after or without infection with BRCA1 shRNA, 16 hr or 8 day after treatment with 2 μM Olaparib, as indicated. See Figure 6 and Table S1.

Cell

Supplemental Information

53BP1 and the LINC Complex Promote Microtubule-Dependent DSB Mobility and DNA Repair

Francisca Lottersberger, Roos Anna Karssemeijer, Nadya Dimitrova, and Titia de Lange

SUPPLEMENTAL EXPERIMENTAL PROCEDURES

Cell lines, cell treatments, plasmids, and shRNAs

SV40LT TRF2$^{F/F}$ Cre-ER^{T1}, TRF2$^{F/F}$ 53BP1$^{-/-}$ and TRF2$^{F/F}$ 53BP1$^{-/-}$ Lig4$^{-/-}$, TRF2$^{F/F}$ Rif1$^{F/F}$ MEFs have been either previously described (Dimitrova et al., 2008; Denchi and de Lange, 2007; Lottersberger et al., 2013; Zimmermann et al., 2013) or were obtained by intercrosses with Cre-ER^{T1} mice (TRF2$^{F/F}$ 53BP1$^{-/-}$ Cre-ER^{T1} and TRF2$^{F/F}$ 53BP1$^{-/-}$ Lig4$^{-/-}$ Cre-ER^{T1}). SUN1$^{+/-}$ and SUN2$^{+/-}$ mice (012715 and 012716, The Jackson Laboratory), PTIP$^{F/+}$ mice (019143, The Jackson Laboratory), and Kif3A$^{F/F}$ mice (gift from P. Igarashi and L.S.W. Goldstein; (Lin et al., 2003)) were used to derive all compound genotypes by standard crosses with TRF2$^{F/F}$, 53BP1$^{+/-}$, Lig4$^{+/-}$, and Rif1$^{F/F}$ mice. All MEFs were isolated from E12.5 embryos. Genotyping was done by Transnetyx Inc. using real time PCR with allele-specific probes. MEFs were immortalized with pBabeSV40LargeT (a gift from G. Hannon) at P2 or 3 and cultured in Dulbecco's Modified Eagle Medium (DMEM) (Cellgro) supplemented with 15% fetal bovine serum (FBS) (Gibco), non-essential amino acids (Gibco), L-glutamine (Gibco), penicillin/streptomycin (Gibco), 50 μM β-mercaptoethanol (Sigma). Cre was induced with 0.5-1 μM 4-OHT or with three infections at 12 h intervals with pMMP Hit&Run Cre retrovirus derived from transfected Phoenix cells as previously described (Celli and de Lange, 2005). For timed experiments, time point 0 was set at the time of addition of 4-OHT or at 12 h after the first Hit&Run Cre infection. For expression of mCherry-53BP1-2-pWZL, EGFP-TRF1-pWZL (Dimitrova et al., 2008), YFP-tubulin ((Beaudouin et al., 2002); subcloned in pLPC), mAG-hGeminin (Davoli et al., 2010), and mutated alleles of 53BP1DB-pMX, 20 μg of plasmid DNA was transfected into Phoenix cells using $CaPO_4$ precipitation as previously described (Wu et al., 2012). The retroviral supernatant was used for six infections at 6-12 h intervals. Cells were selected for 3-5 d in 2-3 μM Hygromycin or 2-6 μM Puromycin. ShRNAs for

Nesprin 4, Kif3A and Kif5B (TRCN0000-195990/184115/090405/090407/106535/091481 Openbiosystem) were introduced with three infections/day (6-12 h intervals) over two days using the pLKO.1 lentiviral vector (Openbiosystem) produced in 293T cells and infected cells were selected for 3-5 d in Puromycin. Taxol (Paclitaxel, Sigma), Nocodazole (M1404, Sigma), and PARP inhibitor (Opalarib, AZD2281, Selleck chemicals) were dissolved in DMSO and added at a final concentration of 20 μM, 1 μg/ml, and 2 μM, respectively.

For the survival assay, BRCA1 shRNA infected cells were plated in a 6-well plate, in duplicate at 10, 100, and 1000 cells per well. After 24 hours, cells were either left untreated or treated with PARP inhibitor at various concentrations and incubated for 7 days. Media was changed after 4 days. After washing with PBS, colonies were fixed and stained for 1 min in a solution containing 50% methanol, 2% Methylene Blue and rinsed with water. Colony numbers were determined using wells with 10-40 colonies and the % survival at each PARPi concentration compared to the untreated cells was calculated.

Immunoblotting

Immunoblotting was perfomed as previously described (Celli and de Lange, 2005) with minor modifications. Cells were lysed in 2X Laemmli buffer at $5X10^3$ cell/μl and the lysate was denatured for 10 min at 95^oC before shearing with an insulin needle. Lysate equivalent to 10^5 cells was resolved using SDS/PAGE and transferred to a nitrocellulose membrane. The following primary antibodies were utilized: TRF2 (1254, rabbit polyclonal); Chk2 (BD 611570; BD Biosciences); 53BP1(100-304A; Novus Biologicals) or (ab175933; ABCAM), human 53BP1 (BD 612522; BD Biosciences), Myc (9B11, mAb 2276; Cell Signaling), SUN1 (ab74758; Abcam), SUN2 (ab87036; Abcam); Kif5B (ab

15705; Abcam); Kif3A (sc135960; Santa Cruz), Anti-Poly(ADP-ribose) (4335; Trevigen), mBRCA1 (a gift from D. M. Livingston).

Live-cell imaging

Dysfunctional telomeres were visualized using mCherry-BP1-2 (h53BP1, 1220-1711aa) as described previously (Dimitrova et al., 2008). Cre-treated TRF2$^{F/F}$ cells were plated onto MatTek glass bottom plates and grown for 2 days before imaging. An hour before imaging, cells were changed into Leibovitz's L-15 medium (Gibco) supplemented with 15% FBS, non-essential amino acids, L-glutamine, penicillin/streptomycin and 50 μM β-mercaptoethanol, and allowed to equilibrate for one hour. For the analysis of irradiation-induced DSBs, cells were plated 1-2 days before imaging, changed into imaging medium, irradiated and let recover for one hour. Imaging was done at 37°C using an environmental chamber using a DeltaVision RT microscope system (Applied Precision) with a PlanApo 60x 1.40 NA objective lens (Olympus America, Inc.). 5 μm Z-stacks at 0.5 μm steps were acquired using SoftWoRx software with 50 msec exposure time, every 30 sec over 10 min (t=20 frames) at 2 x 2 binning with 512 x 512 pixels in final size. Images were deconvolved and 2D-maximum intensity projection images were obtained using SoftWoRx software. Tracking of mCherry-BP1-2 foci was performed with ImageJ software for at least 10 cells per condition. Cells were registered by the StackReg plugin using Rigid Body (Thevenaz et al., 1998). Next, particles were detected and tracked using the Mosaic Particle Detector and Tracker plugin (Sbalzarini and Koumoutsakos, 2005) with the following parameters: radius=1-2 pixels; cutoff=1-2 pixels; percentile=1-6; link range=1; displacement=5 pixels. The x and y coordinates of each trajectory were output for further calculation. Per cell, all mCherry-BP1-2 foci that were continuously tracked for at least 19 of the 20 frames were analyzed. The analysis of the eGFP-TRF1-marked telomeres was similarly conducted using the following parameters:

radius=1 pixels; cutoff=1 pixels; percentile=8-12; link range=1; displacement=5 pixels.

Identification of distorted nuclei

The average x and y values of all the foci was calculated in each frame as the Geometrical Center (GC) and normalized over the $GC_{t=0}$. The distance traveled by the GC between each time points t=b and t=a was calculated as Movement of Geometrical Center

$$MGC_{b-a} = \sqrt{(x^{GC}_{t=b} - x^{GC}_{t=a})^2 + (y^{GC}_{t=b} - y^{GC}_{t=a})^2}$$

and the maximal MGC (MMGC) for each cell was identified. Cells were discarded if their MMGC exceeded the arbitrary threshold of 2, or if their MMGC exceeded the secondary threshold of 1 and another parameter was also above threshold.

The Difference of the Average Distances of all the *i* foci in the cell and $GC_{t=0}$ (ΔAD) between each time points t=b and t=a was calculated as

$$\mathrm{D}AD_{b-a} = \left| \left(\frac{\sum_{i=1}^{n} \sqrt{(x^{i}_{t=b} - x^{GC}_{t=0})^2 + (y^{i}_{t=b} - y^{GC}_{t=0})^2}}{n} \right) - \left(\frac{\sum_{i=1}^{n} \sqrt{(x^{i}_{t=a} - x^{GC}_{t=0})^2 + (y^{i}_{t=a} - y^{GC}_{t=0})^2}}{n} \right) \right|$$

and the maximal ΔAD (MΔAD) for each cell was identified. Cells were discarded if MΔAD exceeded the arbitrary threshold of 2, or if MΔAD exceeded the secondary threshold of 1 and another parameter was also above threshold.

Finally, the trajectories travelled by each focus *i* per cell, relatively to the GC, were normalized to the coordinates $x^{i}_{t=0}$ and $y^{i}_{t=0}$ and projected together on a XY plane. The percentage of foci in each quadrant was calculated for each time frame: Upper Right (UR(%)), Lower Right (LR(%)), Upper Left (UL(%)), Lower Left (LL(%)) and the average of these values during the time-lapse was derived. Laterality (LAT (%)),

Verticality (VER (%)) and Diagonality (DIA (%)) were calculated for each time frame as:

$$LAT(\%) = \left|(((UR(\%) + LR(\%)), 100) - 0.5), 0.5\right| \times 100$$

$$VER(\%) = \left|(((UR(\%) + UL(\%)), 100) - 0.5), 0.5\right| \times 100$$

$$DIA(\%) = \left|(((UR(\%) + LL(\%)), 100) - 0.5), 0.5\right| \times 100$$

and the average of these values during the time-lapse were derived. Cells were discarded if UR, LR, UL, LL, LAT, VER or DIA exceeded the arbitrary threshold of 40%, or if they exceeded the secondary threshold of 30% and another parameter was also above threshold.

The Cumulative Distance traveled in 10 min by each of the foci *i* (CD^i) was calculated relative to the GC, as previously described (Dimitrova et al., 2008), as

$$CD^i = \sum_{t=1}^{20} \sqrt{((x_t^i - x_t^{GC}) - (x_{t-1}^i - x_{t-1}^{GC}))^2 + ((y_t^i - y_t^{GC}) - (y_{t-1}^i - y_{t-1}^{GC}))^2} .$$

Mean Square Displacement (MSD) was calculated as

$$MSD(\Delta t) = \frac{1}{n} \times \sum_{i=1}^{n} D_i(\Delta t)^2 ,$$

where

$$D_i(\Delta t) = \sqrt{((x_t^i - x_t^{GC}) - (x_{t-\Delta t}^i - x_{t-\Delta t}^{GC}))^2 + ((y_t^i - y_t^{GC}) - (y_{t-\Delta t}^i - y_{t-\Delta t}^{GC}))^2} .$$

All data output in pixels (standard ImageJ output) were converted to meters by the formula, 1 pixel = 0.215 μm, based on the characteristics of the objective.

Diffusion Coefficient D was calculated as

$$D = m / 4$$

where *m* is the slope of the MSD after fitting to a linear curve.

Anomalous Diffusion Coefficient α was derive using MATLAB by the fitting of MSD to the diffusion model function:

$$MSD = A + Gt^{a}$$

For cumulative distance, statistical analysis was performed using Prism Software applying the Mann-Whitney test.

IF and IF-FISH

Cells grown on coverslips were fixed for 10 min in 3% paraformaldehyde/2% sucrose at room temperature. IF and IF-FISH were then carried out as previously described (Takai et al., 2003; Dimitrova et al., 2008). Digital images were captured on a Zeiss Axioplan II microscope with a Hamamatsu C4742-95 camera using Volocity software. The following primary antibodies were utilized: 53BP1(100-304A; Novus Biologicals, or ab175933; Abcam), human 53BP1 (BD 612522; BD Biosciences), γH2AX (JBW301; Millipore), Rif1 (1240, rabbit polyclonal; (Buonomo et al., 2009)).

Telomere ChIP

Telomeric ChIP was conducted as previously described (Loayza and de Lange, 2003). The following primary antibodies were utilized: TRF1 (1449, crude serum), 53BP1(ab175933; ABCAM), SUN1 (ab74758; Abcam), SUN2 (ab87036; Abcam).

Analysis of metaphase chromosomes

Telomeres were detected by FISH on metaphase spreads using a previously described protocol (Lansdorp et al., 1996) with minor modifications (Celli and de Lange, 2005; Doksani et al., 2013). Images were acquired using a Zeiss Axioplan II microscope with a Hamamatsu C4742-95 camera using Volocity software. For radial chromosomes, MEFs were incubated with PARPi (2 μM) for 16 h before harvest and the trypsinized cells were incubated in 0.055 M KCl at 37°C for 30 min before being processed.

In-gel analysis of single-stranded telomeric DNA

Mouse telomeric DNA was analyzed on CHEF gels as described previously (Wu et al., 2012).

qRT-PCR Analysis

Nesprin-4 RNA levels were analyzed after RNA isolation and quantitative PCR as described in (Kabir et al., 2014). Differences calculated using the ΔCT method were normalized to GAPDH expression. Primers:

Nesprin-4_FW: TAGCCTGGTGCTTGAGAAGG

Nesprin-4_RV: AGGAGTGGGGAAGGTACTGG

GAPDH_FW: GTGTTCCTACCCCCAATGTGT

GAPDH _RV: ATTGTCATACCAGGAAATGAGCTT

53BP1 alleles and PTIP construct

S/TQ mutants were generated using Gibson cloning using previously published constructs as a template (Bothmer et al., 2011). Briefly, the mutated residues for 53BP1ΔPTIP (S6A, S13A, S25A, S29A) and 53BP1ΔMOB (S674A, T696A, S698A, S784A, S831A, T855A, S892A, S1068A, S1086A, S1104A, T1148A, S1171A, S1219A) were obtained by PCR using 53BP1-28A as a template. The non-mutated residues and vector backbone were generated by PCR using 53BP1DB as the template. To generate the full-length vector, both PCR products were joined using Gibson cloning based on homology from the PCR primers. Primers:

53BP1ΔPTIP_FW: GAAAACAAGGTTGCAGACCCTGTGGATTCTTC;

53BP1ΔPTIP_RV: GAAGAATCCACAGGGTCTGCAACCTTGTTTTC;

53BP1ΔMOB_FW: CAGTTCCGTCACCAGCTACTCGATCTGAGGCAC;

53BP1ΔMOB_RV: GTGCCTCAGATCGAGTAGCTGGTGACGGAACTG;

53BP1Nterm_FW: GGTGGACCATCCTCTAGACTGCCGGATCCGAATTC;

53BP1Nterm_RV: GAATTCGGATCCGGCAGTCTAGAGGATGGTCCACC.

Full-length mouse PTIP was cloned as a BamHI/EcoRI fragment into the pLPC retroviral vector, adding a myc tag to the C terminus.

Coimmunoprecipitation

4-5x10^6 293T cells were plated in a 10 cm dish 20-24 h prior to transfection by $CaPO_4$ precipitation using 10 μg of each plasmid DNA as indicated. Medium was changed 12 hr after transfection and 24-28 h later cells were incubated with zeocin for 20 min, harvested by scraping in cold PBS on ice, and collected by centrifugation. After resuspension in 0.5 ml hypotonic lysis buffer (10% glycerol, 10mM KCl, 10 mM Hepes (pH 7.9), 0.1 mM EDTA, 0.5% NP-40, 1.5 mM $MgCl_2$, Complete protease inhibitor mix (Roche), and PhosSTOP phosphatase inhibitor mix (Roche)), the KCl concentration was raised to 400 mM. Samples were sonicated for 1 min in water bath solicitor and equal amount of lysis buffer, without KCl, was added to reduce KCl concentration to 200 mM. After centrifugation at 16,000 rpm for 10 min at 4°C, samples were incubated with magnetic beads conjugated with anti-FLAG M2 antibody (Sigma) as described (Subbotin and Chait, 2014) and nutated at 4°C for 1 hr. Beads were washed 7 times with the lysis buffer containing 150 mM KCl and immunoprecipitated proteins were eluted with 50 μl of 2xLaemmli buffer. Samples were boiled for 5 min before separation on SDS-PAGE.

SUPPLEMENTAL REFERENCES

Beaudouin, J., Gerlich, D., Daigle, N., Eils, R., and Ellenberg, J. (2002). Nuclear envelope breakdown proceeds by microtubule-induced tearing of the lamina. Cell *108*, 83-96.

Bothmer, A., Robbiani, D. F., Di Virgilio, M., Bunting, S. F., Klein, I. A., Feldhahn, N., Barlow, J., Chen, H. T., Bosque, D., Callen, E., Nussenzweig, A., and Nussenzweig, M. C. (2011). Regulation of DNA end joining, resection, and immunoglobulin class switch recombination by 53BP1. Mol Cell *42*, 319-329.

Buonomo, S., Wu, Y., Ferguson, D., and de Lange, T. (2009). Mammalian Rif1 contributes to replication stress survival and homology-directed repair. J Cell Biol *187*, 385-398.

Celli, G. B., and de Lange, T. (2005). DNA processing is not required for ATM-mediated telomere damage response after TRF2 deletion. Nat Cell Biol *7*, 712-718.

Davoli, T., Denchi, E. L., and de Lange, T. (2010). Persistent telomere damage induces bypass of mitosis and tetraploidy. Cell *141*, 81-93.

Denchi, E. L., and de Lange, T. (2007). Protection of telomeres through independent control of ATM and ATR by TRF2 and POT1. Nature *448*, 1068-1071.

Dimitrova, N., Chen, Y. C., Spector, D. L., and de Lange, T. (2008). 53BP1 promotes non-homologous end joining of telomeres by increasing chromatin mobility. Nature *456*, 524-528.

Doksani, Y., Wu, J. Y., de Lange, T., and Zhuang, X. (2013). Super-resolution fluorescence imaging of telomeres reveals TRF2-dependent T-loop formation. Cell *155*, 345-356.

Kabir, S., Hockemeyer, D., and de Lange, T. (2014). TALEN Gene Knockouts Reveal No Requirement for the Conserved Human Shelterin Protein Rap1 in Telomere Protection and Length Regulation. Cell Rep *9*, 1273-1280.

Lansdorp, P. M., Verwoerd, N. P., van de Rijke, F. M., Dragowska, V., Little, M. T., Dirks, R. W., Raap, A. K., and Tanke, H. J. (1996). Heterogeneity in telomere length of human chromosomes. Hum Mol Genet *5*, 685-691.

Lin, F., Hiesberger, T., Cordes, K., Sinclair, A. M., Goldstein, L. S., Somlo, S., and Igarashi, P. (2003). Kidney-specific inactivation of the KIF3A subunit of kinesin-II inhibits renal ciliogenesis and produces polycystic kidney disease. Proc Natl Acad Sci U S A *100*, 5286-5291.

Loayza, D., and de Lange, T. (2003). POT1 as a terminal transducer of TRF1 telomere length control. Nature *424*, 1013-1018.

Lottersberger, F., Bothmer, A., Robbiani, D. F., Nussenzweig, M. C., and de Lange, T. (2013). Role of 53BP1 oligomerization in regulating double-strand break repair. Proc Natl Acad Sci U S A *110*, 2146-2151.

Sbalzarini, I. F., and Koumoutsakos, P. (2005). Feature point tracking and trajectory analysis for video imaging in cell biology. J Struct Biol *151*, 182-195.

Subbotin, R. I., and Chait, B. T. (2014). A pipeline for determining protein-protein interactions and proximities in the cellular milieu. Mol Cell Proteomics *13*, 2824-2835.

Takai, H., Smogorzewska, A., and de Lange, T. (2003). DNA damage foci at dysfunctional telomeres. Curr Biol *13*, 1549-1556.

Thevenaz, P., Ruttimann, U. E., and Unser, M. (1998). A pyramid approach to subpixel registration based on intensity. IEEE Trans Image Process *7*, 27-41.

Wu, P., Takai, H., and de Lange, T. (2012). Telomeric 3' Overhangs Derive from Resection by Exo1 and Apollo and Fill-In by POT1b-Associated CST. Cell *150*, 39-52.

Zimmermann, M., Lottersberger, F., Buonomo, S. B., Sfeir, A., and de Lange, T. (2013). 53BP1 regulates DSB repair using Rif1 to control 5' end resection. Science *339*, 700-704.